Optical measurement of voltage sensing by endogenous ion channels

Authors

Parashar Thapa[1‡], Robert Stewart[1‡], Rebecka J. Sepela[1], Oscar Vivas[2], Laxmi K. Parajuli[2], Mark Lillya[1], Sebastian Fletcher-Taylor[1,3], Bruce E. Cohen[3], Karen Zito[2], Jon T. Sack[1*]

[1]Department of Physiology and Membrane Biology, University of California, Davis, CA 95616

[2]Center for Neuroscience, University of California, Davis, CA 95616

[3]Molecular Foundry and Division of Molecular Biophysics & Integrated Bioimaging, Lawrence Berkeley National Laboratory, Berkeley, CA 94720

[‡]Authors contributed equally to this work

*Correspondence to jsack@ucdavis.edu

Abstract

A primary goal of molecular physiology is to understand how conformational changes of proteins affect the function of cells, tissues, and organisms. Here, we describe an imaging method for measuring the conformational changes of the voltage sensors of endogenous ion channel proteins within live tissue. We synthesized a fluorescent variant of a peptidyl toxin, that is compatible with two-photon excitation microscopy. This fluorescent probe targets the voltage sensors of Kv2 proteins, which form potassium channels and plasma membrane–endoplasmic reticulum junctions**.** We develop a statistical thermodynamic model to calculate behavior of unlabeled Kv2 voltage sensors from fluorescence images. Two-photon excitation imaging of rat brain slices reveals coupling between membrane potential and the conformation of endogenous neuronal Kv2 proteins. This quantitative imaging method enables measurement of the coupling of conformational state with function of an endogenous protein in tissue, without genetic modification.

Introduction

To move the field of voltage-sensitive physiology forward, we need new tools that indicate when and where voltage-sensitive conformational changes in endogenous proteins occur. Many classes of transmembrane proteins have been found to be voltage sensitive (Bezanilla 2008). One important class of voltage-sensitive proteins is the voltage gated ion channels. Electrophysiological techniques have enabled extensive studies into the voltage-sensitivity of ionic conductances, primarily under reductionist experimental conditions where the channels have been removed from their native tissue. In addition to their canonical function as ion-conducting channels, voltage gated ion channel proteins have nonconducting functions which are independent of their ion conducting functions (Kaczmarek 2006). These nonconducting protein functions are largely inaccessible to study by electrophysiology, and are more poorly understood. Novel approaches are needed to learn more about voltage-sensing in intact tissues and to unlock the mysterious realm of nonconducting voltage-sensitive physiology. Here, we present a new approach to image the conformational changes of endogenous voltage-sensitive proteins in living tissue.

We have developed a new protein imaging tool, an Endogenous Voltage-sensor Activity Probe (EVAP), which dynamically labels living tissue to reveal the spatiotemporal conformational status of endogenous proteins. Here we report synthesis, validation, and measurements using an EVAP which reports the conformational state of the voltage sensor of endogenous Kv2 proteins. Kv2 proteins form voltage-gated K^+ channels, and regulate a wide variety of physiological responses in tissues throughout the body (Bocksteins 2016). Electrophysiological approaches can detect the voltage-sensitive K^+ conductance of Kv2 channels. However, the majority of Kv2 proteins on cell surface membranes do not function as channels, they are nonconducting (Benndorf *et al.* 1994, O'Connell *et al.* 2010, Malin *et al.* 2013). Kv2 proteins dynamically regulate cellular physiology by nonconducting functions (Antonucci *et al.* 2001, Singer-Lahat *et al.* 2007, Feinshreiber *et al.* 2010, X. Q. Dai *et al.* 2012, Fox *et al.* 2015, Johnson *et al.* 2018, Kirmiz, Palacio *et al.* 2018, Kirmiz, Vierra *et al.* 2018, Kirmiz *et al.* 2019, Vierra *et al.* 2019). The Kv2 EVAP reports on the conformation of Kv2 voltage sensors independently from ion conductance, enabling the study of Kv2's nonconducting physiological functions. We present

this EVAP both as a useful research tool, and as a prototype molecular probe for imaging voltage sensing by endogenous proteins, in tissue, with molecular specificity.

Voltage sensor coupling in voltage gated ion channels

Kv2 proteins are members of the voltage-gated cation channel superfamily. The voltage sensors of proteins in this superfamily are comprised of a bundle of four transmembrane helices termed S1-S4 (Long *et al.* 2005, 2007). The S4 helix contains positively charged arginine and lysine residues, gating charges, which respond to voltage changes by moving through the transmembrane electric field (Aggarwal & MacKinnon 1996, Seoh *et al.* 1996, Islas & Sigworth 1999). When voltage sensor domains encounter a transmembrane voltage that is more negative on the inside of the cell membrane, voltage sensors are biased towards resting conformations, or down states, in which gating charges are localized intracellularly. When voltage becomes more positive, gating charges translate towards the extracellular side of the membrane, and voltage sensors are progressively biased towards up states, in a process of voltage activation (Armstrong & Bezanilla 1973, Zagotta *et al.* 1994, Tao *et al.* 2010, Xu *et al.* 2019). Voltage sensor activation is coupled to the conductance gate of voltage gated ion channels, and can also be coupled to nonconducting protein functions. To study the coupling of voltage sensors to these functions, it is essential to measure voltage sensor activation itself. Conformational changes of voltage sensors have been detected with electrophysiological measurements of gating currents (Armstrong & Bezanilla 1973, M. F. Schneider & Chandler 1973, Bezanilla 2018) or by optical measurements from fluorophores covalently attached to voltage sensors by genetic encoding (Lin & Schnitzer 2016) and/or by chemical engineering (G. Zhang *et al.* 2015). However, experimental limitations prevent these existing techniques from measuring conformational changes of voltage sensors of most endogenous proteins: gating currents can only be measured when the proteins are expressed at high density in a voltage-clamped membrane; engineered proteins differ from endogenous channels; and introducing point mutations and conjugated fluorophores into voltage sensors alters structure and function. Here, we develop a different strategy, EVAPs that dynamically label endogenous voltage sensors to reveal conformational states, and apply this strategy to Kv2 proteins.

Kv2 proteins have important nonconducting functions.

Mammals express two Kv2 proteins, Kv2.1 and Kv2.2, which homo- or hetero-tetramerize to form the pore of voltage-gated potassium channels (Frech *et al.* 1989, Trimmer 1991, Kihira *et al.* 2010, Bishop *et al.* 2015). Kv2 proteins contribute to cell physiology in a variety of contexts ranging from neuronal firing (Du *et al.* 2000, Liu & Bean 2014, Speca *et al.* 2014, Hönigsperger *et al.* 2017), visual transduction (Gayet-Primo *et al.* 2018), muscle contraction (H. Xu *et al.* 1999, Amberg & Santana 2006), cell division (Cobb *et al.* 2015), apoptosis (Pal *et al.* 2003), and hormone secretion (Singer-Lahat *et al.* 2007, Feinshreiber *et al.* 2010, X. Q. Dai *et al.* 2012). However, the majority (73% to more than 99%) of the Kv2 proteins on cell surface membranes are nonconducting (Benndorf *et al.* 1994, O'Connell *et al.* 2010, Fox *et al.* 2013). These nonconducting Kv2 proteins have voltage sensor movement that is decoupled from pore opening (Fox *et al.* 2013). The nonconducting functions of Kv2 proteins are an area of intense current interest. Kv2 nonconducting include regulation of plasma membrane–endoplasmic reticulum junctions (Antonucci *et al.* 2001, Fox *et al.* 2015, Johnson *et al.* 2018, Kirmiz, Palacio *et al.* 2018, Kirmiz, Vierra *et al.* 2018), phosphoinositide homeostasis (Kirmiz *et al.* 2019), calcium signaling (Vierra *et al.* 2019), and exocytosis (Singer-Lahat *et al.* 2007, Feinshreiber *et al.* 2010), and insulin secretion (X. Q. Dai *et al.* 2012). Movements of intracellular Kv2 domains are voltage-sensitive (Kobrinsky *et al.* 2006), but the degree of coupling between voltage sensors and Kv2's intracellular binding partners is unclear.

New means are needed to address questions about coupling of voltage sensor movements to native functions. We have designed a molecular tool that enables researchers to image activation of endogenous voltage sensors. Our optical probe selectively reports the conformational state of Kv2 voltage sensors in living tissue, and the functional coupling of voltage sensor movements. Understanding whether voltage sensor movement is coupled to specific functions will establish whether these functions are themselves responsive to membrane potential.

GxTX-594 is a molecular probe that enables investigation of Kv2 voltage sensing in living brain slices.

To image activation of native Kv2 proteins, we exploit the conformation-selective binding of the tarantula peptide guangxitoxin-1E (GxTX) to image where the voltage sensors of Kv2 proteins

adopt a specific resting conformation in tissue. We synthesized GxTX-594, a fluorescent derivative of GxTX that is compatible with two-photon excitation imaging through light-scattering tissue. This EVAP equilibrates with Kv2 proteins on the time scale of seconds, revealing the probability (averaged over time) that unbound voltage sensors are resting or active. We develop a method to calculate the average conformational status of unlabeled Kv2 proteins from images of GxTX-594 fluorescence. We deploy the GxTX-594 probe in brain slices and image voltage-sensitive fluorescence changes that elucidate the spatiotemporal pattern of conformational changes of endogenous neuronal Kv2 proteins. This EVAP approach provides an imaging technique to study conformational changes of voltage-sensitive proteins in samples that have not (or cannot) be genetically modified.

Results

To create an optical probe of Kv2 voltage sensors, we used solid-phase peptide synthesis to generate a variant of GxTX, an amphiphilic 36-amino acid cystine knot peptide. GxTX partitions into the outer leaflet of the plasma membrane bilayer where it selectively binds to membrane-embedded voltage sensors of Kv2 proteins (Milescu *et al.* 2009, Tilley *et al.* 2014, Gupta *et al.* 2015). We synthesized Ser13Cys GxTX, where the free "spinster" thiolate side chain (Shimony *et al.* 1994) of cysteine 13 is predicted to extend into extracellular solution when the peptide is bound to a voltage sensor. GxTX-1E folds by formation of 3 internal disulfides, and cysteine 13 was differentially protected during oxidative refolding to direct chemoselective conjugation (Tilley *et al.* 2014). Following refolding and thiol deprotection, the maleimide derivative of Alexa Fluor 594, a persulfonated Texas Red analog, was condensed with the free thiol, and Ser13Cys(Alexa Fluor 594) GxTX-1E (called "GxTX-594" throughout) was purified and tested for activity against Kv2.1 (Fig. 1 and Fig 1 Supplement 1). These results demonstrate that GxTX-594 retains bioactivity against Kv2 proteins. Alexa Fluor 594 exhibits a large two-photon absorption cross-section and ample spectral separation from green fluorescent protein (GFP), making it well-suited for multiplexed, two-photon excitation imaging experiments (Zito *et al.* 2004).

GxTX-594 colocalizes with Kv2.1 and Kv2.2

We first assessed whether GxTX-594 labels Kv2 proteins. Mammals have two Kv2 pore-forming subunits, Kv2.1 and Kv2.2, both of which are expressed in neurons throughout the brain (Trimmer 1991, Kihira *et al.* 2010, Bishop *et al.* 2015). CHO-K1 cells were transfected with either a rat Kv2.1-GFP or Kv2.2-GFP construct. While the CHO-K1 cell line has little, if any, endogenous K^+ current (Gamper *et al.* 2005), transfection with either Kv2.1-GFP or Kv2.2-GFP yielded delayed rectifier K^+ currents (Fig 6 Supplement 1 A, top two rows). When imaged two days post transfection, Kv2.1-GFP and Kv2.2-GFP fluorescence appeared at the surface membrane of the transfected CHO cells, and the fluorescence was localized predominantly to the glass-adhered basal surface, where it adopted a clustered morphology (Fig 1 A). Clustered basal expression is a hallmark of Kv2 localization in neurons and other mammalian cell lines when they are adhered to glass (Shi *et al.* 1994, Antonucci *et al.* 2001). After incubation with membrane-impermeant GxTX-594 (100 nM for 5 minutes), GxTX-594 fluorescence localized to

regions with Kv2-GFP signal (Fig 1 A). GxTX-594, and Kv2.1-GFP or Kv2.2-GFP, had Pearson correlation coefficients that averaged 0.86 or 0.80, respectively, verifying a high degree of colocalization of both Kv2 proteins with GxTX-594 (Fig 1 B). The ratio of GxTX-594 to GFP fluorescence intensity was similar for Kv2.1-GFP or Kv2.2-GFP (Fig 1 C), consistent with the lack of discrimination of GxTX between Kv2.1 and Kv2.2 (Herrington *et al.* 2006).

GxTX-594 binds Kv2.1 in the presence of its neuronal auxiliary subunit AMIGO-1

In neurons, Kv2 proteins colocalize with an auxiliary subunit, AMIGO-1 (Peltola *et al.* 2011, Bishop *et al.* 2018). AMIGO-1 is a single-pass transmembrane protein with a large extracellular domain, an architecture similar to auxiliary subunits of voltage-gated sodium channels, Kv4 channels, or BK channels that modulate binding of peptide toxins to the channels (Xia *et al.* 1999, Gilchrist *et al.* 2013, Maffie *et al.* 2013). To determine if AMIGO-1 affects GxTX-594 labeling, Kv2.1-expressing cells were transiently transfected with an AMIGO-1-YFP construct. For these experiments, Kv2.1 was expressed in a CHO-K1 cell line stably transfected with rat Kv2.1 under control of a tetracycline-inducible promoter (Kv2.1-CHO) (Trapani & Korn 2003). Kv2.1 expression was induced with minocycline 48 hours prior to experiments, such that all Kv2.1-CHO cells expressed Kv2.1. In this expression system, Kv2.1 is not tagged with a fluorescent protein. AMIGO-1-YFP fluorescence was observed in clusters at the basal membrane (Fig 2 A) similar to Kv2.1-GFP (Fig 1 A). GxTX-594 colocalized with AMIGO-1-YFP (Fig 2 A). Pearson's correlation coefficient indicated colocalization between AMIGO-1-YFP and GxTX-594, consistent with AMIGO-1 colocalizing with clustered Kv2.1 (Fig 2 B). GxTX-594 also labeled cells that did not express AMIGO-1 (Fig 2 A). We tested whether binding of GxTX-594 to Kv2.1 is different between cells which do or do not express AMIGO-1. Increasing concentrations of GxTX-594 were applied to cells and the relationship between GxTX-594 fluorescence intensity and dose was quantified for cells expressing AMIGO-1-YFP (green) and cells not expressing AMIGO-1-YFP (blue) (Fig 2 C). A Langmuir binding isotherm was fit to GxTX-594 fluorescence intensity (lines, Fig 2 D), and resulted in an indistinguishable dissociation constant between cells expressing AMIGO-1-YFP (27 ± 14 nM) and cells not expressing AMIGO-1-YFP (26.9 ± 8.3 nM). Thus, there is no indication that AMIGO-1 disrupts the GxTX-594–Kv2 interaction.

GxTX-594 fluorescence dynamics report Kv2 voltage activation

To understand the relationship between voltage sensor conformational change and GxTX-594 fluorescence, we determined how fluorescence intensity on cells expressing Kv2.1 responds to changes in membrane voltage. For these experiments, Kv2.1-CHO cells were incubated in minocycline for 48 hours to induce Kv2.1 expression. Kv2.1-CHO cells were then incubated for 5 minutes in a bath solution containing 100 nM GxTX-594 before dilution with extracellular solution to 9 nM, and imaged at least 9 minutes after dilution. Fluorescence intensity images were generated from airy disk confocal imaging of cells voltage-clamped in the whole-cell patch clamp configuration. Unlike images shown in Fig 1, the imaging plane for voltage-clamp experiments was above the glass-adhered surface. This higher plane was chosen because GxTX-594 labeling kinetics are slower in the highly restricted extracellular space where the plasma membrane adheres to glass (Fig 3 Supplement 1).

To measure voltage-dependent fluorescence changes, cells were held at -80 mV and stepped to indicated test potentials (Fig 3 A). A region of interest (ROI) corresponding to the cell surface was manually identified and average fluorescence intensity quantified from time-lapse sequences. Average fluorescence intensity from the cell surface was background-subtracted using the average fluorescence intensity from an ROI in a region without cells. Both the amplitude and kinetics of fluorescence change from cell surface ROIs are sensitive to voltage (Fig 3 B), similar to prior findings with GxTX-550 (Tilley *et al.* 2014). We observed that cells exhibited a baseline fluorescence intensity above background, even when given a +80 mV depolarizing voltage stimulus (Fig 3 B). This residual fluorescence varied between cells (Fig 3 C) and was potentially due to internalized GxTX-594 and/or autofluorescence. However, much of the residual fluorescence appeared to be localized to the cell surface membrane (Fig 3 A). As such membrane labeling was not present on CHO cells in the absence of Kv2 proteins (Fig 6), this fluorescence could indicate a population of Kv2.1 that resides at the cell surface and binds GxTX-594 in a fashion that renders the Kv2.1–GxTX complex insensitive to voltage.

To compare labeling intensity between cells, the initial fluorescence at a holding potential of -80 mV was normalized to 100% F/F_{init}, and residual fluorescence after a +80 mV step was normalized to 0% F/F_{init} (Fig 3 D). The fluorescence–voltage response was fit with a Boltzmann

function with a half maximal voltage midpoint ($V_{1/2}$) of -27 mV and a steepness (z) of 1.4 elementary charges (e_0) (Fig 3 D, black line).This is strikingly similar to the voltage dependence of integrated gating charge from Kv2.1-CHO cells, without any GxTX present $V_{1/2}$ = -26 mV, z = 1.6 e_0 (Tilley *et al.* 2019).

To determine the temporal response of GxTX-594 labeling to voltage change, we compared rates of fluorescence change ($k_{\Delta F}$) to varying step potentials (Fig 3 E) in the same data set that were analyzed in Fig 3 D. We quantified rates of fluorescence change ($k_{\Delta F}$) by fitting a monoexponential function:

$$F = F_\infty + F_0 e^{\frac{(t-t_0)}{\tau}} \quad \text{(Equation 1)}$$

Where $\tau = 1/k_{\Delta F}$, t = time, t_0 = time at start of fit, F = fluorescence intensity, F_0 = fluorescence at start of fit, F_∞ = fluorescence after infinite time. In response to voltage steps from a holding potential of -80 mV to more positive potentials, $k_{\Delta F}$ increased progressively from approximately -40 mV to +40 mV. After a return to -80 mV, labeling occurred at a rate similar to unlabeling at -40 mV, indicating that the rate of relaxation to a labeled/unlabeled equilibrium saturates below -40 mV. There was substantial variability in $k_{\Delta F}$ between cells (Fig 3 E). We wondered if this could be due to fluctuations in ambient temperature (27-29°C), given the substantial temperature sensitivity reported for Kv2.1 conductance (F. Yang & Zheng 2014). However the temperature dependence of $k_{\Delta F}$ indicated that only 1.3-fold variation could be attributed to a 2°C temperature variation (Fig 3 Supplement 2), suggesting that there are determinants of $k_{\Delta F}$ variability which are intrinsic to individual cells. The $k_{\Delta F}$–voltage response was fit with a Boltzmann distribution (Eq. 2) resulting in $V_{1/2}$ = +2 mV and z = 1.1 e_0 (Fig 3 E, black line). Notably, the dynamic fluorescence responses of GxTX-594 to voltage changes occurred at physiologically relevant potentials, suggesting that changes in GxTX-594 labeling intensity or rate could occur in response to changes in cellular electrical signaling.

The relation between voltage sensor activation and GxTX-594 dynamics can be recapitulated by rate theory modeling.

To enable translation of the intensity of fluorescence from GxTX-594 on a cell surface into a measure of conformational change, we developed a model relating cell labeling to voltage sensor activation. The framework of this model is generalizable to fluorescent molecular probes that

report conformational changes by a change in binding affinity. In our model of EVAP labeling, the ratio of labeled to unlabeled Kv2 in a membrane is determined by confomational change from resting to activated altering the binding and unbinding rates of the EVAP (Scheme I).

Scheme I

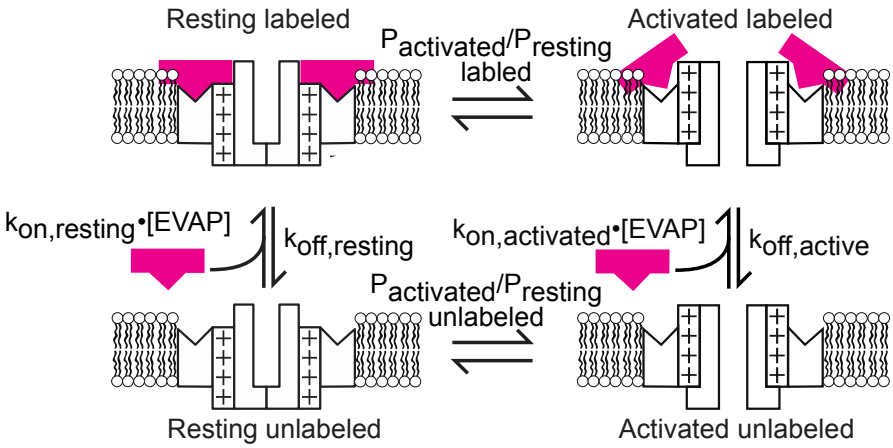

Scheme II

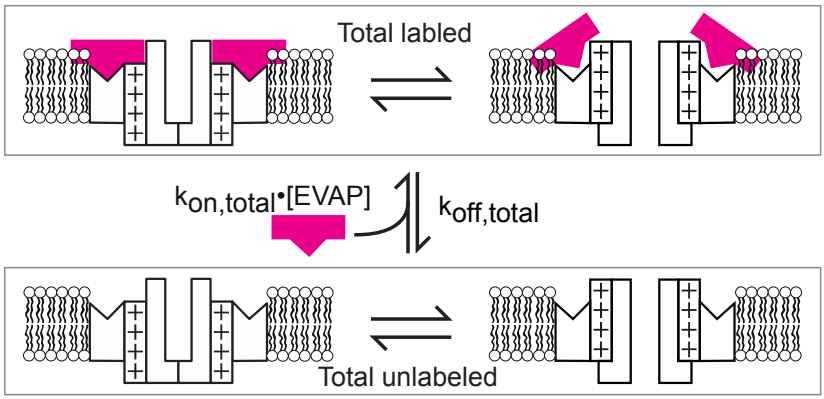

The Scheme I model assumes the innate voltage sensitivity of the Kv2 subunit is solely responsible for controlling voltage dependence. Labeling is voltage-dependent because the binding and unbinding rates are different for resting and activated conformations of voltage sensors. When voltage sensors change from resting to activated conformations, the binding rate of the EVAP decreases and the unbinding rate increases. When the membrane voltage is held constant for sufficient time, the proportions of labeled and unlabeled proteins reach an equilibrium. Scheme I assumes that voltage sensor conformational changes equilibrate much faster than EVAP binding or unbinding, such that binding and unbinding are the rate-limiting steps. EVAP labeling requires seconds to equilibrate (Fig 3), whereas Kv2 channel gating equilibrates in milliseconds (Tilley *et al.* 2019), three orders of magnitude more quickly. This

much faster voltage sensor equilibration justifies our simplifying approximation that voltage sensor conformations achieve equilibrium so quickly that only their distribution at equilibrium impacts the kinetics of labeling and unlabeling. Voltage-activation of Kv2 channels involve many conformational changes (Scholle *et al.* 2004, Jara-Oseguera *et al.* 2011, Tilley *et al.* 2019). However, models which presume independent activation of a voltage sensor in each of the four Kv2.1 subunits accurately predict many aspects of voltage activation and voltage sensor toxin binding (Lee *et al.* 2003, Tilley *et al.* 2019). Thus, we found it reasonable to model voltage sensor activation of Kv2 proteins as a single, rapid transition of each voltage sensor from a resting conformation to an activated conformation. With this model, at any given voltage, there is a probability that a voltage sensor is either in its resting conformation ($P_{resting}$), or in its activated conformation ($P_{activated}$), such that $P_{activated} = (1 - P_{resting})$. The equilibrium for voltage sensor activation is then a ratio of activated to resting voltage sensors ($P_{activated}/P_{resting}$) in which

$$\frac{P_{activated}}{P_{resting}} unlabeled = e^{(V - V_{1/2,unlabeled})\frac{zF}{RT}} \qquad \text{Equation 2a}$$

$$\frac{P_{activated}}{P_{resting}} labeled = e^{(V - V_{1/2,labeled})\frac{zF}{RT}} \qquad \text{Equation 2b}$$

where $V_{1/2}$ is the voltage where $P_{activated}/P_{resting,} = 1$, z is the number of elementary charges determining voltage dependence, F is the Faraday constant, R is the ideal gas constant, and T is absolute temperature. In a prior study, we fit the conductance–voltage relation of Kv2.1 with a Boltzmann distribution that yielded $V_{1/2}$ = -31.7 mV with $z = 1.5\ e_0$ for the early movement of 4 independent voltage sensors, and found that with a saturating concentration of GxTX the $V_{1/2}$ = 41.3 mV (Tilley *et al.* 2019, Fig. 1 C). These values were used for $V_{1/2,unlabled}$, z, and $V_{1/2,labled}$ respectively (Table 1). To relate voltage sensor activation to labeling and unlabeling, we used microscopic binding ($k_{on}[EVAP]$) and unbinding (k_{off}) rates that are distinct for resting and activated voltage sensors. We estimated values for these rates assuming

$$k_{\Delta F} = k_{on}[EVAP] + k_{off} \qquad \text{(Equation 3)}$$

and

$$K_d = \frac{k_{off}}{k_{on}} \qquad \text{(Equation 4)}$$

To calculate the $k_{on,resting}$ and $k_{off,resting}$ values reported in Table 1, we used the saturating value at negative voltages of the $k_{\Delta F}$–voltage relation (Fig 3 E), and K_d from dose-response imaging (Fig 2 D). In 9 nM GxTX-594, at greater than +40 mV, voltage-dependent unlabeling was nearly complete, indicating that $k_{off,activated} >> k_{on,activated}[EVAP]$. We input the saturation of $k_{\Delta F}$ at positive voltages as $k_{off,activated}$ (Fig 3 E). The slow labeling of activated voltage sensors confounded attempts to measure $k_{on,activated}$ directly, and we used the statistical thermodynamic principle of microscopic reversibility (Lewis 1925) to constrain $k_{on,activated}$:

$$\frac{\frac{P_{activated}}{P_{resting}},labeled}{\frac{P_{activated}}{P_{resting}},unlabeled} = \frac{\frac{k_{off,resting}}{k_{on,resting}}}{\frac{k_{off,activated}}{k_{on,activated}}} \qquad \text{(Equation 5)}$$

At any static voltage, the simplifying assumption that voltage sensors are in continuous equilibrium allows Scheme I to collapse into Scheme II, which has only a single microscopic binding rate, $k_{on,total}[EVAP]$, and unbinding rate, $k_{off,total}$. In Scheme II, $k_{on,total}$ is a weighted sum of both $k_{on,resting}$ and $k_{on,activated}$ from Scheme I. The weights for $k_{on,total}$ are the relative probabilities that unlabeled voltage sensors are resting or activated, which is determined at any static voltage by an equilibrium constant, $\frac{P_{activated}}{P_{resting}} unlabeled$:

$$k_{on,total} = k_{on,resting}[EVAP] \cdot \frac{1}{1+\frac{P_{activated}}{P_{resting}} unlabeled} + k_{on,active}[EVAP] \cdot \frac{1}{1+\frac{1}{\frac{P_{activated}}{P_{resting}} unlabeled}}$$

(Equation 6)

Similarly, $k_{off,total}$ is determined by the unbinding rate from resting voltage sensors ($k_{off,resting}$) and the unbinding rate from activated voltage sensors ($k_{off,activated}$), and weighted such that:

$$k_{off,total} = k_{off,resting} \cdot \frac{1}{1+\frac{P_{activated}}{P_{resting}} labeled} + k_{off,active} \cdot \frac{1}{1+\frac{1}{\frac{P_{activated}}{P_{resting}} labeled}} \qquad \text{(Equation 7)}$$

Using $k_{on,total}$ and $k_{off,total}$ we can compute $k_{\Delta F}$ using Equation 3. To test the predictive value of the Scheme II model, we compared the predicted $k_{\Delta F}$ to experimental measurements in 9 nM GxTX-594 (Fig 3 E, blue line). We found the Scheme II model reasonably reproduced the voltage dependence of Kv2.1 labeling.

The Scheme II model was also used to predict the magnitude of EVAP fluorescence changes on cell surfaces. In theory, the ratio of fluorescence at a test voltage to a prior voltage (F/F_{init}) is equal to the probability that a Kv2 subunit is labeled by the EVAP ($P_{lableled}$):

$$\frac{F}{F_{init}} = \frac{P_{labeled}}{P_{labeled,init}} \qquad \text{(Equation 8)}$$

The equilibrium $P_{labeled}$ at any voltage can be determined from microscopic binding rates associated with Scheme II where:

$$P_{labeled} = \frac{1}{1+\frac{K_{d,total}}{[EVAP]}} = \frac{1}{1+\frac{k_{off,total}}{k_{on,total}\cdot[EVAP]}} \qquad \text{(Equation 9)}$$

Using this model, we calculated the fluorescence–voltage relation from $P_{labeled}$ (Equation 8) and compared these calculated values to our experimental data. The model predicts fluorescence response within the range of the experimental data (Fig 3 D, blue line).

Rate theory modeling roughly predicts GxTX-594 labeling during dynamic voltage changes

The Scheme II model relating labeling to voltage sensor activation was developed for static voltages. However, in electrically activated cells, voltage is dynamic. In neurons, action potentials involving Kv2 currents occur on the millisecond time scale (Liu & Bean 2014, Kimm *et al.* 2015), orders of magnitude faster than the GxTX-594 response. Thus, the slow EVAP response will integrate voltage fluctuations occurring over many seconds. The Scheme II model assumes that voltage sensors are in continuous equilibrium, and this assumption breaks down when voltage is rapidly changing, as Kv2 voltage sensor movements with or without GxTX require milliseconds to equilibrate (Tilley *et al.* 2019). We assessed whether the Scheme II model retains predictive power in response action potentials by stimulating cells with brief

voltage steps that crudely mimic action potentials. We stimulated GxTX-594 labeled Kv2.1-CHO cells with trains of 2 ms voltage steps from -80 to +40 mV, and observed a change in cell surface fluorescence (Fig 4 A, B). To assess frequency response, step frequency was varied from 0.02 to 200 Hz. At frequencies higher than 25 Hz, detectable unlabeling occurred (Fig 4 C), and $k_{\Delta F}$ varied with stimulus frequency (Fig 4 D). Frequency-dependent predictions of F/F_{init} and $k_{\Delta F}$ were made from the Scheme II model. These predictions were calculated assuming the summed probability of being at every voltage determines the overall $P_{labeled}$. The general form of our equation relating fluorescence intensity change to a stimulus that varies faster than EVAP labeling is:

$$F/F_{init} = (P_{V1} \cdot \Delta F_{V1}) + (P_{V2} \cdot \Delta F_{V2}) + \ldots + (P_{Vn} \cdot \Delta F_{Vn}) \qquad \text{(Equation 10)}$$

where ΔF_n is ΔF at that particular voltage. For voltage steps from -80 to +40 mV Eq. 10 is:

$$F/F_{init} = (P_{40mV} \cdot \Delta F_{40mV}) + (P_{-80mV} \cdot \Delta F_{-80mV})$$

Measured changes in fluorescence intensity were 2- to 3-fold more sensitive to frequency than responses predicted by the Eq. 10 (Fig 4 C, blue line). When the fluorescence intensity changes were fit with a Boltzmann distribution, the fit had a similar slope but the midpoint was at a lower stimulus frequency than the model predictions (Fig 4 C, black line). This discrepancy could be due to Kv2.1 voltage sensors having insufficient time to equilibrate at high stimulus frequencies. The time constant of deactivating gating current decay from Kv2.1-CHO cells was 22 ms at -80 mV (Tilley *et al.* 2019). Voltage sensors that fail to deactivate before the next stimulus could lead to an accumulation of activated voltage sensors, and more EVAP unlabeling than predicted by Eq. 10 which assumes continuous equilibrium.

The general form of our equation relating fluorescence intensity change to a stimulus that varies faster than EVAP labeling is:

$$k_{\Delta F} = \left(P_{V1} \cdot k_{\Delta F,V1}\right) + \left(P_{V2} \cdot k_{\Delta F,V2}\right) + \ldots + (P_{Vn} \cdot k_{\Delta F,Vn}) \qquad \text{(Equation 11)}$$

where P_{Vn} is the probability over time that the voltage has a particular value and $k_{\Delta F,n}$ is $k_{\Delta F}$ at that particular voltage. For voltage steps from -80 to +40 mV Eq. 11 is:

$$k_{\Delta F} = (P_{40mV} \cdot k_{\Delta F40mV}) + (P_{-80mV} \cdot k_{\Delta F-80mV})$$

The model produced a frequency dependence of $k_{\Delta F}$ that was within range of the empirical data (Fig 4 D, blue line).

Overall, the response of GxTX-594 labeling to rapidly varying stimuli indicates that the fluorescence response generally follows the predictions of the Scheme II model, although GxTX-594 labeling is more sensitive to high frequency stimulation than predicted. As this very simple model recapitulated the general response of an EVAP to static and varying voltage stimuli, we further investigated its predictions of EVAP labeling responses and its utility in interpreting changes in EVAP labeling.

Changes in EVAP labeling report conformational changes of unlabeled Kv2 proteins.

We used the EVAP model to investigate general principles of the relation between voltage sensor activation and labeling. In particular, we are interested in exploiting EVAP labeling to reveal information about voltage sensor activation in the unlabeled Kv2 population, akin to how Ca^{2+} indicators are used to reveal the concentration of free Ca^{2+}. The Scheme I model was used to predict labeling at a series of EVAP concentrations (Fig 5 A). While the model was calibrated to fluorescence responses at particular voltages (Fig 5 A, bottom axis), EVAP labeling is not directly sensitive to voltage, but is determined by the probability that voltage sensors are in an activated conformation (Fig 5 A, top axis). As the EVAP binds resting voltage sensors much more rapidly than activated voltage sensors ($k_{on,resting} >> k_{on,activated}$) the probability that unlabeled voltage sensors are resting determines the labeling rate, and influences P_{bound}. Our model predicts that as the EVAP concentration decreased, the change in labeling ($\Delta F/\Delta F_{max}$) asymptotically approaches the probability that unlabeled voltage sensors are resting (Fig 5 A). Even at 100 nM GxTX-594, more than 3 times the K_d for the resting conformation, a change in labeling corresponds to a conformational change in the voltage sensors of unlabeled Kv2 proteins. At and below the K_d for the resting conformation, the change in labeling was nearly

proportionate with voltage sensor conformational change. The predicted rate of fluorescence change ($k_{\Delta F}$) approaches a consistent response as EVAP concentration decreased below the K_d for the resting conformation. Thus, the fluorescence response is similar at EVAP all concentrations below the K_d for the resting conformation, when a minority of EVAP binding sites are occupied. This indicates that if the concentration of EVAP applied to a tissue is below the K_d for the resting conformation, EVAP dynamics are expected to be consistent throughout a tissue, even if the EVAP concentration is lower due to difficulty penetrating tissue or is otherwise depleted. Overall, a broad qualitative interpretation can be made from EVAP fluorescence changes: a change in labeling indicates that voltage sensors of unlabeled Kv2 proteins have changed their probability of being activated.

GxTX-594 selectively labels Kv2 proteins

Armed with a model for interpretation of changes in EVAP labeling, we proceed to determine whether GxTX-594 could reveal conformational changes of endogenous Kv2 proteins. An important consideration in interpreting fluorescence images of tissues is whether cell labeling with the GxTX-594 EVAP could be due to receptors other than Kv2 proteins. Electrophysiological studies have concluded that the native GxTX peptide is selective for Kv2 channels, with some off-target modulation of A-type Kv4 channels (Herrington *et al.* 2006, Liu & Bean 2014, Speca *et al.* 2014). However, electrophysiological testing only indicates whether GxTX modulates channels; electrophysiology cannot detect ligands that bind proteins, but do not alter currents (Sack *et al.* 2013). Furthermore, structural differences between wild-type GxTX and the GxTX-594 variant could potentially alter selectivity among channel protein subtypes.

To test whether GxTX-594 binds other voltage-gated K^+ channel subtypes, we quantified surface labeling and analyzed colocalization of GxTX-594 with a selection of GFP-labeled voltage-gated K^+ channel subtypes. A series of GFP-K^+ channel protein fusions were identified that express and retain function with a GFP tag: rat Kv4.2-GFP (Shibata *et al.* 2003), rat Kv1.5-GFP (Li *et al.* 2001), and mouse BK-GFP. Transfection of each of these channel subtypes into CHO cells resulted in voltage-dependent outward currents, consistent with cell surface expression of the K^+ channels (Fig 6, Supplement 1 A). In imaging analysis, the surface membrane was identified by labeling with a fluorescent wheat germ agglutinin (WGA) conjugate. Transfection of all K^+

channel-GFP constructs resulted in GFP localization at the cell surface, however the majority of the Kv4.2 and Kv1.5 appeared intracellularly retained (Fig 6, Supplement 1 B). Consistent with reports in other cell lines, cell surface localization improved when of Kv4.2 was co-transfected with KChIP2 (Shibata *et al.* 2003) or Kv1.5 with Kvβ2 (Shi *et al.* 1996) (Fig 6 A). After incubation with 100 nM GxTX-594 for five minutes, cells expressing the GFP-tagged variants of Kv2.1 and 2.2 became labeled while neither Kv4.2 + KChIP2, nor Kv1.5 + Kvβ2, nor BK channels were appreciably labeled (Fig 6 A). When the background-subtracted GxTX-594:GFP fluorescence intensity ratio was normalized to GxTX-594:Kv2.1-GFP, this ratio was close to zero for Kv4.2 + KChIP2, Kv1.5 + Kvβ2, or BK (Fig 6 B), suggesting minimal binding to these channel subtypes. Furthermore, no colocalization was apparent between Kv4.2 + KChIP2, Kv1.5 + Kvβ2, or BK and GxTX-594 (Fig 6 C). A similar set of experiments conducted without the auxiliary subunits of Kv4.2 or Kv1.5 also gave no indication of GxTX-594 labeling of Kv4.2 or Kv1.5 (Fig 6, Supplement 1 B, C, D). We did not conduct a comprehensive survey of all the more than 80 known mammalian proteins containing voltage sensor domains, and thus cannot be certain that GxTX-594 does not bind any other voltage sensors, or other receptors on cell surfaces. However, the lack of labeling of these related voltage-gated K^+ channels indicates that GxTX-594 does not promiscuously label voltage sensors. In all tests conducted, GxTX-594 was selective for Kv2 proteins.

To determine whether expression of Kv2 proteins embedded in tissue can be imaged with GxTX-594, we overexpressed Kv2.1-GFP in brain slices. We examined rat brain at CA1 pyramidal neurons of the hippocampus. CA1 neurons express Kv2 channels, the physiology of these neurons have been intensively studied, and their electrical properties are relatively homogeneous (Misonou *et al.* 2005). Organotypic hippocampal slice cultures prepared from postnatal day 5-7 rats were sparsely transfected with Kv2.1-GFP, resulting in a subset of neurons displaying green fluorescence. When imaged two to four days after transfection, GFP fluorescence was observed in the plasma membrane surrounding neuronal cell bodies and proximal dendrites (Fig 7 Supplement 1 A and B). Six days or more after transfection, Kv2.1-GFP fluorescence organized into clusters on the surface of the cell soma and proximal processes (Fig 7 A, Fig 7 Supplement 1 C), a pattern consistent with a prior report of endogenous Kv2.1 in CA1 neurons (Misonou *et al.* 2005). After identifying a neuron expressing Kv2.1-GFP, solution flow into the imaging

chamber was stopped and GxTX-594 was added to the static bath solution to a final concentration of 100 nM. After five minutes of incubation, solution flow was restarted, leading to wash-out of GxTX-594 from the imaging chamber. After wash-out, GxTX-594 fluorescence remained colocalized with Kv2.1-GFP (Fig 7, Fig 7 Supplement 1), indicating that GxTX-594 is able to permeate through dense neural tissue and bind to Kv2 proteins on neuronal surfaces. Pearson correlation coefficients confirmed the colocalization of GxTX-594 with Kv2.1-GFP in multiple slices (Fig 7 C). In most images of Kv2.1-GFP expressing neurons, GxTX-594 labeled puncta were observed on neighboring neurons that did not express Kv2.1-GFP, but at intensities that were roughly an order of magnitude dimmer (Fig 7 B, white arrow). The similarity in the labeling patterns are consistent with GxTX-594 labeling endogenous Kv2 proteins. The lack of GxTX-594 labeling of non-Kv2 K^+ channels, the increased labeling of neurons where Kv2.1-GFP is expressed, and the Kv2-like labeling patterns of CA1 neurons all indicate that GxTX-594 selectively labels Kv2 proteins in living brain slices.

GxTX-594 labeling of neurons in brain slice responds to neuronal depolarization

To test whether GxTX-594 labeling of neurons in brain slices is consistent with labeling of endogenous Kv2 voltage sensors, we determined whether GxTX-594 labeling responds to voltage changes. First, we looked for Kv2-like labeling patterns on CA1 pyramidal neurons in untransfected brain slices bathed in 100 nM GxTX-594. In two-photon excitation optical sections thinner than the neuronal cell bodies, fluorescent puncta circumscribed dark intracellular spaces (Fig 8 A). This was similar to the patterns of fluorescence in Kv2.1-GFP transfected slices (Fig 7 B), and consistent with the punctate expression pattern of Kv2.1 in CA1 pyramidal neurons seen in fixed brain slices (Misonou *et al.* 2005).

We tested whether the punctate fluorescence was voltage-sensitive using voltage clamp. To ensure voltage clamp of the neuronal cell body, slices were bathed in tetrodotoxin to block Na^+ channels, and Cs^+ was included in the patch pipette solution to block K^+ currents. In each experiment, whole-cell configuration was achieved from a GxTX-594 labeled neuron, and holding potential was set to -70 mV. At this point, time-lapse imaging of a two-photon excitation optical section was initiated. Depolarization to 0 mV resulted in loss of fluorescence from a subset of puncta at the perimeter of the voltage-clamped neuron (Fig 8 B red arrows,

Supplemental Movie). Other fluorescent puncta appeared unaltered by the 0 mV step (Fig 8 B, white arrows).

To assess if the apparent stimulus-dependent fluorescence decrease noted in puncta after a voltage step to 0 mV was due to random fluctuations during imaging, we compared fluorescence of the apparent cell membrane region to regions more distal from the voltage-clamped cell body. To quantify this fluorescence change, an ROI 30 pixels (1.2 μm) wide containing the apparent membrane of the cell body was compared to other regions within each image (Fig 8 C). The region containing the membrane of the cell body lost fluorescence during the 0 mV step (Fig 8 D, ROI 1) while neither of the regions more distal (ROI 2, ROI 3), nor the intracellular region (ROI 0) showed a similar change. In multiple slices, the voltage-dependent decrease of fluorescence was seen specifically in the region of the voltage-clamped neuronal membrane (Fig 8 E). The kinetics of fluorescence response of the voltage-clamped membrane region were similar between slices (Fig 8 F).

To determine whether the fluorescence response to depolarization was driven by the Kv2-like puncta on the cell membrane, the fluorescence along a path containing the apparent cell membrane was selected by drawing a path connecting fluorescent puncta surrounding the dark cell body region, and averaging fluorescence in a region 10 pixels wide (0.4 μm) centered on this path (Fig 8 G, yellow line). The fluorescence intensity along the path of the ROI revealed distinct peaks corresponding to puncta (Fig 8 H, red trace). After stepping the neuron to 0 mV, the intensity of fluorescence of a subset of puncta lessened (Fig 8 H, black trace, peaks 1,3,4,5,8). The Scheme II model predicts a 55% reduction of fluorescence, but even more reduction is observed in individual fluorescence puncta in brain slice (Fig 8, I blue line). This would be expected if the concentration of GxTX-594 diminished as it penetrated into the brain tissue (Fig 6 A). In addition to the depolarization-responsive fluorescence puncta, other puncta which appeared to be on the surface of the same cell body, maintained or increased their brightness after depolarization (Fig 8 H, black trace, peaks 2, 6, 7). These puncta could represent Kv2 proteins on a neighboring cell, internalized Kv2-GxTX-594 complexes, off-target labeling by GxTX-594, or Kv2 proteins that are unresponsive to voltage. When the kinetics of fluorescence intensity decay of individual voltage-sensitive puncta were fit with Eq. 1, $k_{\Delta F}$ values were similar

between puncta (Fig 8 I), consistent with these spatially separated puncta all being on the surface of the voltage-clamped neuron. The fluorescence changes measured in these puncta were similar to those predicted by the Figure 6 model (Fig 8 I, blue line). To address whether the fluorescence change at the cell membrane was driven by decreases in regions of punctate fluorescence, the punctate and non-punctate fluorescence intensity changes were analyzed separately. The regions with fluorescence intensities above average for the path (Fig 8 H, dashed line) were binned as one group. The above-average group, by definition, contained all punctate fluorescence. When comparing the fluorescence before and during the 0 mV step, the regions that were initially below average maintained the same intensity (103 ± 8%); regions of above average fluorescence decreased in the intensity (70 ± 8%) (Fig 8 J). This suggests that the detectable unlabeling along the cell membrane originated in the Kv2-like puncta, not the regions of lower fluorescence intensity between them.

To determine whether the dynamics of voltage-dependent response of GxTX-594 fluorescence on neurons in brain slices were consistent with labeling of Kv2.1, we performed experiments with Kv2.1-expressing CHO cells under similar conditions as brain slice: 100 nM GxTX-594, 30°C, Cs^+-containing patch pipette solution. The rate of fluorescence changes in Kv2.1-CHO cells were similar to neurons in brain slices, and consistent with the $k_{\Delta F}$ of 0.06 s^{-1} predicted by Figure 6 model (Fig 8 K). The data indicate that the voltage sensors of Kv2 proteins in hippocampal CA1 neurons have a similar response to voltage as the voltage-sensitive Kv2.1 proteins in CHO cells.

Discussion

We conclude that GxTX-594 dynamically labels a resting conformation of endogenous Kv2 proteins in neurons. This conclusion is based on a series of findings: GxTX-594 labels Kv2 proteins (Fig 1) in the presence of its obligate neuronal auxiliary subunit AMIGO-1 (Fig 2), but does not label related Kv proteins (Fig 6). Steps to 0 mV resulted in dynamic unlabeling of CHO cells (Fig 3) and neurons (Fig 8), with similar kinetics (Fig 8 K). The punctate GxTX-594 labeling of CA1 neurons is consistent with the patterns of endogenous Kv2 expression seen by immunofluorescence (Misonou *et al.* 2005, Bishop *et al.* 2015, 2018), and Kv2.1-GFP expression (Fig 7). These results are consistent with the GxTX-594 probe labeling endogenous Kv2 in rat CA1 hippocampal pyramidal neurons and unlabeling in response to voltage activation. This is an important result demonstrating that an EVAP approach can reveal conformational changes of molecularly specified voltage sensor subtypes, in tissue, with subcellular resolution. Below, we discuss scientific questions that could be addressed with GxTX-594, limitations of GxTX-594, and the potential for engineering mechanistically related probes to report activity of other endogenous proteins.

Unique capabilities of GxTX-594

The Kv2 EVAP presented here is the only imaging method we are aware of for measuring voltage-sensitive conformational changes of a specific, endogenous protein. The molecular, conformational, and spatial precision of fluorescence from GxTX-594 demonstrates its utility for identifying where in tissue the conformational status of Kv2 voltage sensors becomes altered. GxTX-594 labels the fully resting conformation of the Kv2 voltage sensor, in which the first gating charge of the Kv2 S4 segment is expected to be in the gating charge transfer center (Tao *et al.* 2010). Images of GxTX-594 fluorescence reveal this conformation's occurrence, with subcellular spatial resolution. Importantly, the thermodynamic model we develop allows deconvolution of the behavior of unlabeled Kv2 proteins from Kv2 proteins inhibited by GxTX-594.

Our results indicate that the majority of Kv2 protein clustered at an individual plasma membrane–endoplasmic reticulum junction can be voltage sensitive. This consistent with an earlier proposal that, in rat CA1 neurons, clustered Kv2.1 proteins remain voltage sensitive, but

voltage sensing is decoupled from pore opening (Fox *et al.* 2013). Interestingly, when Kv2.1 is overexpressed in CHO cells, a fraction of the Kv2.1-associated GxTX-594 fluorescence is voltage insensitive (Fig 4C). This observation is consistent with voltage sensor immobilization in some surface-expressed Kv2.1 proteins. A similar phenomenon has been noted with the L-type Ca^{2+} channel Cav1.2, which has some gating charge immobilized until it is bound by an intracellular protein (Turner *et al.* 2019).

We used images of GxTX-594 fluorescence to measure the coupling between endogenous Kv2 proteins and membrane potential at specific, subcellular anatomical locations. This demonstrates that GxTX-594 enables measurement of coupling membrane voltage to Kv2 voltage sensor conformational change. Furthermore, if other cellular perturbations are coupled to Kv2 voltage sensors, they as well should affect GxTX-594 labeling. Thus, GxTX-594 imaging could enable studies of a host of questions about the voltage sensitivity of the nonconducting functions of Kv2 proteins, including: formation of plasma membrane–endoplasmic reticulum junctions (Antonucci *et al.* 2001, Fox *et al.* 2015, Kirmiz, Palacio *et al.* 2018), regulation of exocytosis (Singer-Lahat *et al.* 2007, Feinshreiber *et al.* 2010), regulation of insulin secretion (X. Q. Dai *et al.* 2012), interaction with kinases, phosphatases and SUMOylases (Misonou *et al.* 2004, Park *et al.* 2006, X.-Q. Dai *et al.* 2009, Cerda & Trimmer 2011, McCord & Aizenman 2013), formation of specialized subcellular calcium signaling domains (Vierra *et al.* 2019), and interactions with astrocytic end feet (Du *et al.* 1998). Imaging GxTX-594 while perturbing any of these functions could reveal coupling to Kv2 voltage sensors. Beyond the nervous system, Kv2 proteins are coupled to a wide variety of physiological responses in organs throughout the body including muscle, thymus, spleen, kidney, adrenal gland, pancreas, lung, and reproductive organs (Bocksteins 2016). Imaging GxTX-594 with functional measurements from these tissues could reveal how Kv2 proteins couple voltage changes to their many physiological outputs.

Limitations of GxTX-594

The selectivity for a specific conformation of the Kv2 target protein, and the spatial precision of fluorescence from GxTX-594, appear to be near theoretical limits. However, the temporal resolution of GxTX-594 is far slower than the kinetics of Kv2 conformational change, limiting measurements to the probability, averaged over time, that voltage sensors are resting or active.

The probability of a conformation's occurrence is a valuable measure, and the ultimate quantitation of many biophysical studies of ion channels (e.g., open probability, steady state conductance, gating charge-voltage relation). The kinetics of GxTX-594 labeling are compatible with measuring changes in Kv2 activity on a time scale of tens of seconds. We have demonstrated that the temporal resolution of GxTX-594 is compatible with live imaging and electrophysiology experiments.

Fluorescence signal intensity limits interpretation of EVAP labeling. We found that the intensity of GxTX-594 labeling of CA1 neurons was sufficient to report voltage sensing of their endogenous Kv2 proteins. This result demonstrates that GxTX-594 labeling can be implemented a tissue that expresses Kv2 proteins. Kv2 proteins are expressed by most neurons, and many non-neuronal cell types throughout the body (Bocksteins 2016). We expect that GxTX-594 imaging could be implemented in most brain regions. CA1 hippocampal neurons express Kv2 proteins at a density typical of central neurons (Misonou *et al.* 2004, Vacher *et al.* 2008, Speca *et al.* 2014). In other cell types, such as neurons of the subiculum, or the inner segment of photoreceptors, Kv2 proteins are expressed at far higher densities (Maletic-Savatic *et al.* 1995, Gayet-Primo *et al.* 2018). Improved signal to noise would be expected from such cells that express higher densities of Kv2 proteins.

GxTX-based probes inhibit the Kv2 proteins they label. Thus, GxTX-594 depletes the population of Kv2 proteins responding normally to physiological stimuli. While the concentration of an EVAP can be lowered to minimize interference with Kv2 activity, fluorescence intensity is diminished and further limits the ability to detect subtle physiological changes. With a related probe, we explored the impact of simultaneously decreasing toxin concentration and stimulating with physiological stimuli (Tilley *et al.* 2014). Here, we demonstrate that lower concentration and physiological stimuli are not always required for scientifically meaningful implementation of the probe. Even when using GxTX-594 concentrations that grossly interfere with activity, the behavior of unlabeled Kv2 proteins can be calculated using thermodynamic model we have developed.

A limitation of the analysis developed here is that the model of Kv2 voltage sensor conformational change is an oversimplification. The gating dynamics of Kv2 channels are more complex than our model (Islas & Sigworth 1999, Scholle *et al.* 2004, Jara-Oseguera *et al.* 2011, Tilley *et al.* 2019). Under some conditions the assumption of voltage sensor independence may limit the model's predictive power. Additionally, the model of GxTX-594 labeling developed here assumes that voltage sensors are in continuous equilibrium. These deviations from equilibrium could explain the deviation of the model from the data in response to high frequency voltage steps (Fig 4 C, D).

Conformation-selective probes reveal conformational change of endogenous proteins

Measurements of dynamic labeling by a conformation-selective probe such as GxTX can enable deduction of how unlabeled proteins behave. This is perhaps counterintuitive because GxTX inhibits voltage sensor movement of the Kv2 protein it binds, and thus only the bound protein generate optical signals (Tilley *et al.* 2014, 2019). This approach is analogous to calcium imaging experiments, which have been spectacularly informative about physiological calcium signaling (W. Yang & Yuste 2017), despite the fact that no optical signals originate from the physiologically relevant free Ca^{2+}, only from Ca^{2+} that is chelated by a dye. In all such experiments, fluorescence from Ca^{2+}-bound dyes is deconvolved using the statistical thermodynamics of Ca^{2+} binding to calculate free Ca^{2+} (Adams 2010). Similarly, GxTX-based probes dynamically bind to unlabeled Kv2 proteins, and the binding rate is dependent on the probability that unlabeled voltage sensors are in a resting conformation (Fig 5). Thus, the conformations of unlabeled Kv2 proteins influence the dynamics of labeling with GxTX-based probes. Consequently, the dynamics of labeling reveal the conformations of unlabeled Kv2 proteins.

Deployment of GxTX-594 to report conformational changes of endogenous proteins demonstrates that conformation-selective ligands can be used to image occurrence of the conformations they bind to. The same principles of action apply to any conformation-selective labeling reagent, suggesting that probes for conformational changes of many different proteins could be developed. Probes could conceivably be developed from the many other voltage sensor toxins and other gating modifiers that act by a similar mechanism as GxTX, yet target the

voltage sensors of different ion channel proteins (McDonough *et al.* 1997, Sack *et al.* 2004, Catterall *et al.* 2007, Swartz 2007, Schmalhofer *et al.* 2008, Peretz *et al.* 2010, McCormack *et al.* 2013, Ahuja *et al.* 2015, A. H. Zhang *et al.* 2018, Dockendorff *et al.* 2018). Conformation-selective binders have been engineered for a variety of other proteins, and methods to quantify conformational changes from their fluorescence are needed. For example, fluorescently-labeled conformation-selective binders have revealed that endocytosed GPCRs continue to remain in a physiologically activated conformation (Irannejad *et al.* 2013, Tsvetanova *et al.* 2015, Eichel & von Zastrow 2018). A means to determine the conformational equilibria of GPCRs from fluorescence images has not yet been developed. We suggest that the statistical thermodynamic framework developed here could provide a starting point for more quantitative interpretation of other conformation-selective molecular probes.

Materials and methods

GxTX-594 synthesis

The Ser13Cys GxTX peptide synthesized as described (Tilley *et al.* 2014). Methionine 35 of GxTX was replaced by the oxidation-resistant noncanonical amino acid norleucine and serine 13 was replaced with cysteine to create a spinster thiol. Ser13Cys GxTX was labeled with a Texas red derivative (Alexa Fluor 594 C_5 maleimide, Thermo Fisher Scientific, Catalog # 10256). Ser13Cys GxTX lyophilisate was brought to 560 μM in 50% ACN + 1 mM Na_2EDTA. 2.4 μL of 1M Tris (pH 6.8 with HCl), 4 μL of 10 mM of Alexa Fluor 594 C_5 maleimide in DMSO and 17.9 μL of 560 μM Ser13Cys GxTX were added for a final solution of 100 mM Tris, 1.6 mM Alexa Fluor 594 C_5 maleimide and 0.4 mM GxTX in 24 μL of reaction solution. Reactants were combined in a 1.5 mL low protein binding polypropylene tube (LoBind, Eppendorf, Catalog # 022431081) and mixed at 1000 RPM, 20°C for 4 hours (Thermomixer 5355 R, Eppendorf). After incubation, the tube was centrifuged at 845 RCF for 10 minutes at room temperature. A purple pellet was observed post-centrifugation. The supernatant was transferred to a fresh tube and centrifuged at 845 RCF for 10 minutes. After this 2nd centrifugation, no visible pellet was seen. The supernatant was injected onto a reverse-phase HPLC C_{18} column (Biobasic- 4.6mm RP-C_{18} 5 μm, Thermo Fisher Scientific, Catalog # 2105-154630) equilibrated in 20% ACN, 0.1% TFA at 1 mL/min and eluted with a protocol holding in 20% ACN for 2 minutes, increasing to 30% ACN over 1 minute, then increasing ACN at 0.31% per minute. HPLC effluent was monitored by fluorescence and an absorbance array detector. 1 ml fractions were pooled based on fluorescence (280 nm excitation, 350 nm emission) and absorbance (214 nm, 280 nm, and 594 nm). GxTX-594 peptide-fluorophore conjugate eluted at approximately 35% ACN, and mass was confirmed by mass spectrometry using a Bruker UltraFlextreme MALDI-TOF/TOF (Fig 1 Supplement 1). Samples for identification from HPLC eluant were mixed 1:1 in an aqueous solution of 25% MeOH and 0.05% TFA saturated with alpha-cyano-4-hydrocinnamic acid, pipetted onto a ground-steel plate, dried under vacuum, and ionized with 60-80% laser power. Molecular species were detected using a reflector mode protocol and quantitated using Bruker Daltonics flexAnalysis 3.4. Lyophilizate containing GxTX-594 conjugation product was dissolved in CE buffer (defined below), and stored at -80 °C. GxTX-594 concentration was determined by 280 nm absorbance using a calculated extinction coefficient of 18,900 A.U. M^{-1} cm^{-1}.

1

2 ***CHO cell methods***

3 *CHO cell culture and transfection*

4 The CHO-K1 cell line (ATCC) and a subclone transfected with a tetracycline-inducible rat
5 Kv2.1 construct (Kv2.1-CHO) (Trapani & Korn 2003), were cultured as described previously
6 (Tilley *et al.* 2014). To induce Kv2.1 expression in Kv2.1-TREx-CHO cells, 1 μg/mL
7 minocycline (Enzo Life Sciences, Catalog # ALX-380-109-M050), prepared in 70% ethanol at 2
8 mg/mL, was added to the maintenance media to induce K^+ expression. Minocycline was added
9 40-48 hours before imaging and voltage clamp fluorometry experiments. Transfections were
10 achieved with Lipofectamine 2000 (Life Technologies, Catalog # 1668027). 1.1 μL of
11 Lipofectamine was diluted, mixed, and incubated in 110 μL of Opti-MEM (Gibco, Product
12 Number 31985-062, Lot Number 1917064) in a 1:100 ratio for 5 minutes at room temperature.
13 Concurrently, 1 μg of plasmid DNA and 110 μL of Opti-MEM were mixed in the same fashion.
14 DNA and Lipofectamine 2000 mixtures were combined, titurated, and let sit for 20 minutes.
15 Then, the transfection cocktail mixture was added to a 35 mm cell culture dish of CHO cells at
16 approximately 40% confluency and allowed to settle at 37°C 5% CO_2 for 4-6 hours before the
17 media was replaced. Rat Kv2.1-GFP (Antonucci *et al.* 2001), rat Kv2.2-GFP (Kirmiz, Vierra *et*
18 *al.* 2018), rat Kv1.5-GFP (Li *et al.* 2001), rat Kv4.2-GFP (Shibata *et al.* 2003), mouse BK-GFP
19 (Trimmer Lab, UC Davis), rat Kv2.1 S586A-GFP (Kirmiz, Palacio *et al.* 2018), rat AMIGO-
20 YFP (Bishop *et al.* 2015), rat KvBeta2 (Shibata *et al.* 2003) and rat KCHiP2 (An *et al.* 2000)
21 plasmids were all kind gifts from James Trimmer, University of California, Davis. Identities of
22 constructs were confirmed by sequencing from their CMV promoter.

23

24 *Confocal and Airy disk imaging*

25 Confocal images were obtained with an inverted confocal system (Zeiss LSM 880 410900-247-
26 075) run by ZEN black v2.1. A 63x/1.40 NA Oil DIC objective (Zeiss 420782-9900-799) was
27 used for most imaging experiments; a 63x/1.2 NA Water DIC objective (Zeiss 441777-9970-
28 000) was used for voltage clamp fluorometry experiments. GFP and YFP were excited with the
29 488 nm line from an argon laser (3.2 mW at installation) powered at 0.5% unless otherwise
30 noted. GxTX594 was excited with 594 nm helium-neon laser (0.6 mW at installation) powered at
31 10% unless otherwise noted. WGA-405 was excited with a 405 nm diode laser, (3.5 mW at

installation) powered at 1% unless otherwise noted. Temperature inside the microscope housing was 27-30 °C.

In confocal imaging mode, fluorescence was collected with the microscope's 32-detector gallium arsenide phosphide detector array arranged with a diffraction grating to measure 400-700 nm emissions in 9.6 nm bins. Emission bands were 495-550 nm for GFP and YFP, 605-700 nm for GxTX-594, and 420-480 nm for WGA-405. Point spread functions were calculated using ZEN black software using emissions from 0.1 μm fluorescent microspheres, prepared on a slide according to manufacturer's instructions (Thermo Fisher Scientific, Catalog # T7279). The point spread functions for confocal images with the 63x/1.40 Oil DIC objective in the X-Y direction were 228 nm (488 nm excitation) and 316 nm (594 nm excitation).

In Airy disk imaging mode, fluorescence was collected with the microscope's 32-detector gallium arsenide phosphide detector array arranged in a concentric hexagonal pattern (Zeiss Airyscan 410900-2058-580). After deconvolution, the point spread functions for the 63x/1.40 NA objective with 488 nm excitation was 124 nm in X-Y and 216 nm in Z; with 594 nm excitation 168 nm in X-Y and 212 nm in Z. For the 63x/1.2 NA objective, the point spread function with 488 nm excitation was 187 nm in X-Y and 214nm in Z; the point spread function with 594 nm excitation was 210 nm in X-Y and 213 nm in Z.

Unless stated otherwise, cells were plated in uncoated 35 mm dishes with a 7 mm inset No. 1.5 coverslip (MatTek, Catalog # P35G-1.5-20-C). The CHO cell external (CE) solution used for imaging and electrophysiology contained (in mM): 3.5 KCl, 155 NaCl, 10 HEPES, 1.5 $CaCl_2$, 1 $MgCl_2$, adjusted to pH 7.4 with NaOH. Measured osmolarity was 315 mOsm. When noted, solution was supplemented with either 10 mM glucose (CEG) or 10 mM glucose and 1% BSA (CEGB).

For time-lapse, GxTX-594 dose-response experiments, Kv2.1-CHO cells were plated onto 22 x 22 mm No. 1.5H coverglass (Deckglaser). Prior to imaging, cell maintenance media was removed and replaced with CEGB, then coverslip was mounted on an imaging chamber (Warner Instrument, Catalog # RC-24E) with vacuum grease. During time-lapse imaging, indicated

concentrations of GxTX-594 were applied for 10 minutes followed by manual wash-out with CEGB solution. 15 minutes after wash-out, the next GxTX-594 concentration was added. Solutions were added to the imaging chamber perfusion via a syringe at a flow rate of ~1 mL / 10 sec. Images were taken every 5 sec. Laser power was set to 0.5% for the 488 nm laser and 1.5% for the 594 nm laser. For colocalization experiments with GFP-tagged proteins, cells were incubated in 100 nM GxTX-594 for 5 minutes and then washed with CEGB before imaging.

Whole cell voltage clamp for CHO cell imaging

Kv2.1-TREx-CHO cells plated in glass-bottom 35 mm dishes were washed with CEGB, placed in the microscope, and then incubated in 100 µL of 100 nM GxTX594 for 5 minutes to label cells. Before patch clamp, the solution was diluted with 1 mL of CEG for a working concentration of 9 nM GxTX594 during experiments. Cells with obvious GxTX-594 surface staining were voltage-clamped in whole-cell mode with an EPC-10 patch clamp amplifier (HEKA) run by Patchmaster software, v2x90.2 (HEKA). The patch pipette contained a potassium-deficient Cs^+ internal pipette solution to limit outward current and reduce voltage error: 70 mM CsCl, 50 mM CsF, 35mM NaCl, 1 mM EGTA, 10 mM HEPES, brought to pH 7.4 with CsOH. Osmolarity was 310 mOsm. The liquid junction potential was calculated to be 3.5 mV and was not corrected. Borosilicate glass pipettes (Sutter Instruments, Catalog # BF 150-110-10HP) were pulled with blunt tips to resistances less than 3.0 MΩ in these solutions. Cells were held at -80 mV (unless noted otherwise) and stepped to indicated voltages. The voltage step stimulus was maintained until any observed change in fluorescence was complete. For stimulus-frequency dependence experiments, cells were given 2 ms steps to 40 mV at stated frequencies (0.02, 5, 10, 20, 50, 100, 150, or 200 Hz). Images for voltage clamp fluorometry were taken in Airy disk imaging mode with the settings described above.

Whole cell voltage clamp for CHO cell K^+ current recordings

Whole-cell voltage clamp was used to measure currents from CHO cells expressing Kv2.1-GFP, Kv2.2-GFP, Kv1.5-GFP, Kv4.2-GFP, BK-GFP or GFP that we transfected as described above. Cells were plated on glass bottom dishes. Cells were held at -80 mV, then 100 ms voltage steps were delivered ranging from -80 mV to +80 mV in +5 mV increments. Pulses were repeated every 2 seconds. The external (bath) solution contained CE solution. The internal (pipette)

solution contained (in mM): 35 KOH, 70 KCl, 50 KF, 50 HEPES, 5 EGTA adjusted to pH 7.2 with KOH. Liquid junction potential was calculated to be 7.8 mV and was not corrected. Borosilicate glass pipettes (Sutter Instruments, Cat # BF150-110-10HP) were pulled into pipettes with resistance less than 3 MΩ for patch clamp recording. Recordings were at room temperature (22–24 °C). Voltage clamp was achieved with an Axon Axopatch 200B amplifier (MDS Analytical Technologies) run by Pachmaster software, v2x90.2 (HEKA). Holding potential was -80 mV. Capacitance and Ohmic leak were subtracted using a P/5 protocol. Recordings were low pass filtered at 10 kHz and digitized at 100 kHz. Voltage clamp data were analyzed and plotted with Igor Pro 7 or 8 (Wavemetrics). Current amplitudes at each voltage were the average from 0.19-0.20 s after voltage step. As the experiments plotted in Figure 6 Supplement 1 A were merely to confirm functional expression of ion channels at the cell surface, series resistance compensation was not used and substantial cell voltage errors are predicted during these experiments.

Brain slice methods

Hippocampal slice culture preparation and transfection

All experimental procedures were approved by the University of California Davis Institutional Animal Care and Use Committee and were performed in strict accordance with the Guide for the Care and Use of Laboratory Animals of the NIH. Animals were maintained under standard light–dark cycles and had ad libitum access to food and water. Organotypic hippocampal slice cultures were prepared from postnatal day 5-7 rats, as described (Stoppini *et al.* 1991) and detailed in a video protocol (Opitz-Araya & Barria 2011). DIV15-30 neurons were transfected 2-6 days before imaging via biolistic gene transfer (160 psi, Helios gene gun, Bio-Rad), as described in a detailed video protocol (Woods & Zito 2008). 10 µg of plasmid was coated to 6-8 mg of 1.6 µm gold beads.

Two-photon excitation slice imaging

Image stacks (512 x 512 pixels, 1 mm Z-steps; 0.035 µm/pixel) were acquired using a custom two-photon excitation microscope (Olympus LUMPLFLN 60XW/IR2 objective, 60x, 1.0 NA) with two pulsed Ti:sapphire lasers (Mai Tai: Spectra Physics) tuned to 810 nm (for GxTX-594 imaging) and 930 nm (for GFP imaging) and controlled with ScanImage (Pologruto *et al.* 2003).

After identifying a neuron expressing Kv2.1-GFP, perfusion was stopped and GxTX-594 was added to the static bath solution to a final concentration of 100 nM. After five minutes incubation, perfusion was restarted, leading to wash-out of GxTX-594 from the slice bath. Red and green photons (Chroma: 565dcxr, BG-22 glass, HQ607/45) emitted from the sample were collected with two sets of photomultiplier tubes (Hamamatsu R3896).

Whole cell voltage clamp for brain slice imaging

Organotypic hippocampal slice cultures (DIV 6-7, not transfected) were transferred to an imaging chamber with recirculating ACSF maintained at 30°C. To hold the slice to the bottom of the chamber, a horseshoe-shaped piece of gold wire was used to weight the membrane holding the slice. ACSF contained (in mM) 127 NaCl, 25 $NaHCO_3$, 25 D-glucose, 2.5 KCl, 1.25 NaH_2PO_4, 1 MgCl2, 2 $CaCl_2$, 200 nM tetrodotoxin, pH 7.3 and aerated with 95% O_2/ 5% CO_2 (~310mOsm). 4 mL of 100 nM GxTX-594 in ACSF were used in the circulating bath to allow the toxin to reach the slice and reach the desired concentration of 100 nM throughout the circulating bath. Images were acquired beginning 3 minutes after GxTX-594 was added. Apparent CA1 neurons with GxTX-594 labeling in a Kv2-like pattern were selected for whole-cell patch clamp. Voltage clamp was achieved using an Axopatch 200B amplifier (Axon Instruments) controlled with custom software written in Matlab (MathWorks, Inc.). Patch pipettes (5-7 MΩ) were filled with intracellular solution containing (in mM): 135 Cs-methanesulfonate, 10 Na_2-phosphocreatine, 3 Na-L-ascorbate, 4 NaCl, 10 HEPES, 4 $MgCl_2$, 4 Na_2ATP, 0.4 NaGTP, pH 7.2. Neurons were clamped at -70 mV. Input resistance and holding current were monitored throughout the experiment. Cells were excluded if the pipette series resistance was higher than 25 MΩ or if the holding current exceeded -100 pA. To activate Kv2 channels, a 50 s depolarizing step from -70 mV to 0 mV was given.

Image analysis

Fluorescence images were analyzed using ImageJ 1.52n software (C. A. Schneider *et al.* 2012). Regions of interest (ROIs) encompassed the entire fluorescent region of an individual cell or neuron, unless mentioned otherwise. ROIs were drawn manually. Analysis of images was conducted independently by multiple researchers who produced similar results, but analysis was not conducted in a blinded nor randomized fashion. Fluorescence intensity (F) was background

subtracted using mean F of a region lacking cells. For F/F_{init} normalization, F_{init} was the mean fluorescence preceding the indicated voltage stimuli, or the max observed intensity in dose response experiments. Further details of specific normalization procedures are provided in figure legends. Time dependence of fluorescence intensity was fit with a monoexponential decay (Eq. 1). For colocalization analyses the Pearson coefficient was calculated using the JACoP plugin (Bolte & Cordelières 2006). Colocalization analyses were conducted within ROIs defining individual cells. Plotting and curve fitting was performed with with Igor Pro 7 or 8 (Wavemetrics), which performs nonlinear least-squares fits using a Levenberg-Marquardt algorithm. Sample sizes of $n \geq 3$ were selected to confirm reproducibility. Sample sizes of $n \geq 6$ were selected to power nonparametric statistical comparisons to discern $p < 0.01$. Error values from individual curve fittings are standard deviations. All other errors, including error bars, indicate standard errors. Arithmetic means are reported for intensity measurements and correlation coefficients. Geometric means are reported for time constants and rates. As the distributions underlying variability in results are unknown, nonparametric statistical comparisons were conducted with Mann-Whitney U tests and two-tailed p values reported individually if $p > 0.0001$.

Model calculations

Predictions of the Scheme I and II models were calculated using Microsoft Excel. A spreadsheet containing model calculations that can be used to generate model prediction is included as a supplement (Model Calculation Supplement).

Acknowledgements

We thank James Trimmer (University of California, Davis) for numerous discussions, and constructive critical reading of an early version of the manuscript. We thank Georgeann Sack (Afferent, LLC) for critical reading, editing, and feedback. This research was supported by US National Institutes of Health grants R01NS096317 (B.E.C. and J.T.S.), U01NS090581, R21EY026449, and T32GM007377. P. Thapa was supported by American Heart Association postdoctoral fellowship 17POST33670698. Work at the Molecular Foundry was supported by the Director, Office of Science, Office of Basic Energy Sciences, Division of Materials Sciences and Engineering, of the U.S. Department of Energy under Contract No. DE-AC02-05CH11231. The authors declare no competing financial interests.

Author contributions (CRediT nomenclature)

Parashar Thapa: Conceptualization, Formal analysis, Investigation, Methodology, Visualization, Writing- original draft, Writing- reviewing & editing

Robert Stewart: Conceptualization, Formal analysis, Investigation, Methodology, Visualization, Writing- original draft, Writing- reviewing & editing

Rebecka J. Sepela: Conceptualization, Formal analysis, Investigation, Methodology, Visualization, Writing- original draft, Writing- reviewing & editing

Oscar Vivas: Investigation, Methodology, Writing- reviewing & editing

Laxmi K. Parajuli: Investigation, Methodology, Writing- reviewing & editing

Mark Lillya: Conceptualization, Formal analysis, Investigation, Methodology, Visualization

Sebastian Fletcher-Taylor: Investigation, Methodology, Writing- reviewing & editing

Bruce E. Cohen: Conceptualization, Funding acquisition, Project administration, Supervision, Writing- reviewing & editing

Karen Zito: Conceptualization, Funding acquisition, Investigation, Methodology, Project administration, Supervision, Writing- original draft, Writing- reviewing & editing

Jon T. Sack: Conceptualization, Formal analysis, Funding acquisition, Investigation, Methodology, Project administration, Supervision, Visualization, Writing- original draft, Writing- reviewing & editing

References

Adams, S.R. (2010) How calcium indicators work. *Cold Spring Harbor Protocols*, **2010**, pdb.top70. doi:10.1101/pdb.top70

Aggarwal, S.K. & MacKinnon, R. (1996) Contribution of the S4 segment to gating charge in the Shaker K+ channel. *Neuron*, **16**, 1169–77. doi:10.1016/S0896-6273(00)80143-9

Ahuja, S., Mukund, S., Deng, L., Khakh, K., Chang, E., Ho, H., Shriver, S., Young, C., Lin, S., Johnson, J.P., Wu, P., Li, J., Coons, M., Tam, C., Brillantes, B., Sampang, H., Mortara, K., Bowman, K.K., *et al.* (2015) Structural basis of Nav1.7 inhibition by an isoform-selective small-molecule antagonist. *Science*, **350**, aac5464. doi:10.1126/science.aac5464

Amberg, G.C. & Santana, L.F. (2006) Kv2 channels oppose myogenic constriction of rat cerebral arteries. *American Journal of Physiology. Cell Physiology*, **291**, C348-56. doi:10.1152/ajpcell.00086.2006

An, W.F., Bowlby, M.R., Betty, M., Cao, J., Ling, H.P., Mendoza, G., Hinson, J.W., Mattsson, K.I., Strassle, B.W., Trimmer, J.S. & Rhodes, K.J. (2000) Modulation of A-type potassium channels by a family of calcium sensors. *Nature*, **403**, 553–556. doi:10.1038/35000592

Antonucci, D.E., Lim, S.T., Vassanelli, S. & Trimmer, J.S. (2001) Dynamic localization and clustering of dendritic Kv2.1 voltage-dependent potassium channels in developing hippocampal neurons. *Neuroscience*, **108**, 69–81. doi:10.1016/S0306-4522(01)00476-6

Armstrong, C.M. & Bezanilla, F. (1973) Currents related to movement of the gating particles of the sodium channels. *Nature*, **242**, 459–61. doi:10.1038/242459a0

Benndorf, K., Koopmann, R., Lorra, C. & Pongs, O. (1994) Gating and conductance properties of a human delayed rectifier K+ channel expressed in frog oocytes. *The Journal of Physiology*, **477**, 1–14, John Wiley & Sons, Ltd (10.1111). doi:10.1113/jphysiol.1994.sp020166

Bezanilla, F. (2008, April) How membrane proteins sense voltage. *Nature Reviews Molecular Cell Biology*, Nature Publishing Group. doi:10.1038/nrm2376

Bezanilla, F. (2018) Gating currents. *The Journal of General Physiology*, **150**, 911–932. doi:10.1085/jgp.201812090

Bishop, H.I., Cobb, M.M., Kirmiz, M., Parajuli, L.K., Mandikian, D., Philp, A.M., Melnik, M., Kuja-Panula, J., Rauvala, H., Shigemoto, R., Murray, K.D. & Trimmer, J.S. (2018) Kv2 Ion Channels Determine the Expression and Localization of the Associated AMIGO-1 Cell Adhesion Molecule in Adult Brain Neurons. *Frontiers in Molecular Neuroscience*, **11**, 1. doi:10.3389/fnmol.2018.00001

Bishop, H.I., Guan, D., Bocksteins, E., Parajuli, L.K., Murray, K.D., Cobb, M.M., Misonou, H., Zito, K., Foehring, R.C. & Trimmer, J.S. (2015) Distinct Cell- and Layer-Specific Expression Patterns and Independent Regulation of Kv2 Channel Subtypes in Cortical Pyramidal Neurons. *The Journal of Neuroscience*, **35**, 14922–42. doi:10.1523/JNEUROSCI.1897-15.2015

Bocksteins, E. (2016) Kv5, Kv6, Kv8, and Kv9 subunits: No simple silent bystanders. *The Journal of General Physiology*, **147**, 105–25. doi:10.1085/jgp.201511507

Bolte, S. & Cordelières, F.P. (2006) A guided tour into subcellular colocalization analysis in light microscopy. *Journal of Microscopy*, **224**, 213–32. doi:10.1111/j.1365-2818.2006.01706.x

Catterall, W.A., Cestèle, S., Yarov-Yarovoy, V., Yu, F.H., Konoki, K. & Scheuer, T. (2007) Voltage-gated ion channels and gating modifier toxins. *Toxicon*, **49**, 124–141. doi:10.1016/j.toxicon.2006.09.022

Cerda, O. & Trimmer, J.S. (2011) Activity-dependent phosphorylation of neuronal Kv2.1 potassium channels by CDK5. *The Journal of Biological Chemistry*, **286**, 28738–48. doi:10.1074/jbc.M111.251942

Cobb, M.M., Austin, D.C., Sack, J.T. & Trimmer, J.S. (2015) Cell Cycle-dependent Changes in Localization and Phosphorylation of the Plasma Membrane Kv2.1 K+ Channel Impact Endoplasmic Reticulum Membrane Contact Sites in COS-1 Cells. *The Journal of Biological Chemistry*, **290**, 29189–201. doi:10.1074/jbc.M115.690198

Dai, X.Q., Kolic, J., Marchi, P., Sipione, S. & Macdonald, P.E. (2009) SUMOylation regulates Kv2.1 and modulates pancreatic beta-cell excitability. *Journal of Cell Science*, **122**, 775–9. doi:10.1242/jcs.036632

Dai, X.Q., Manning Fox, J.E., Chikvashvili, D., Casimir, M., Plummer, G., Hajmrle, C., Spigelman, A.. F., Kin, T., Singer-Lahat, D., Kang, Y., Shapiro, A.. M.J., Gaisano, H.Y., Lotan, I. & Macdonald, P.E. (2012) The voltage-dependent potassium channel subunit Kv2.1 regulates insulin secretion from rodent and human islets independently of its electrical function. *Diabetologia*, **55**, 1709–20. doi:10.1007/s00125-012-2512-6

Dockendorff, C., Gandhi, D.M., Kimball, I.H., Eum, K.S., Rusinova, R., Ingólfsson, H.I., Kapoor, R., Peyear, T., Dodge, M.W., Martin, S.F., Aldrich, R.W., Andersen, O.S. & Sack, J.T. (2018) Synthetic Analogues of the Snail Toxin 6-Bromo-2-mercaptotryptamine Dimer (BrMT) Reveal That Lipid Bilayer Perturbation Does Not Underlie Its Modulation of Voltage-Gated Potassium Channels. *Biochemistry*, **57**, 2733–2743. doi:10.1021/acs.biochem.8b00292

Du, J., Haak, L.L., Phillips-Tansey, E., Russell, J.T. & McBain, C.J. (2000) Frequency-dependent regulation of rat hippocampal somato-dendritic excitability by the K+ channel subunit Kv2.1. *The Journal of Physiology*, **522 Pt 1**, 19–31. doi:10.1111/j.1469-7793.2000.t01-2-00019.xm

Du, J., Tao-Cheng, J.-H., Zerfas, P. & McBain, C.J. (1998) The K+ channel, Kv2.1, is apposed to astrocytic processes and is associated with inhibitory postsynaptic membranes in hippocampal and cortical principal neurons and inhibitory interneurons. *Neuroscience*, **84**, 37–48. doi:10.1016/S0306-4522(97)00519-8

Eichel, K. & Zastrow, M. von. (2018) Subcellular Organization of GPCR Signaling. *Trends in Pharmacological Sciences*, **39**, 200–208. doi:10.1016/j.tips.2017.11.009

Feinshreiber, L., Singer-Lahat, D., Friedrich, R., Matti, U., Sheinin, A., Yizhar, O., Nachman, R., Chikvashvili, D., Rettig, J., Ashery, U. & Lotan, I. (2010) Non-conducting function of the Kv2.1 channel enables it to recruit vesicles for release in neuroendocrine and nerve cells. *Journal of Cell Science*, **123**, 1940–1947. doi:10.1242/jcs.063719

Fox, P.D., Haberkorn, C.J., Akin, E.J., Seel, P.J., Krapf, D. & Tamkun, M.M. (2015) Induction of stable ER-plasma-membrane junctions by Kv2.1 potassium channels. *Journal of Cell Science*, **128**, 2096–105. doi:10.1242/jcs.166009

Fox, P.D., Loftus, R.J. & Tamkun, M.M. (2013) Regulation of Kv2.1 K(+) conductance by cell surface channel density. *The Journal of Neuroscience*, **33**, 1259–70. doi:10.1523/JNEUROSCI.3008-12.2013

Frech, G.C., VanDongen, A.M.J., Schuster, G., Brown, A.M. & Joho, R.H. (1989) A novel potassium channel with delayed rectifier properties isolated from rat brain by expression cloning. *Nature*, **340**, 642–645. doi:10.1038/340642a0

Gamper, N., Stockand, J.D. & Shapiro, M.S. (2005) The use of Chinese hamster ovary (CHO) cells in the study of ion channels. *Journal of Pharmacological and Toxicological Methods*,

51, 177–85. doi:10.1016/j.vascn.2004.08.008
Gayet-Primo, J., Yaeger, D.B., Khanjian, R.A. & Puthussery, T. (2018) Heteromeric KV2/KV8.2 Channels Mediate Delayed Rectifier Potassium Currents in Primate Photoreceptors. *The Journal of Neuroscience*, **38**, 3414–3427. doi:10.1523/JNEUROSCI.2440-17.2018
Gilchrist, J., Das, S., Petegem, F. Van & Bosmans, F. (2013) Crystallographic insights into sodium-channel modulation by the β4 subunit. *Proceedings of the National Academy of Sciences of the United States of America*, **110**, E5016-24. doi:10.1073/pnas.1314557110
Gupta, K., Zamanian, M., Bae, C., Milescu, M., Krepkiy, D., Tilley, D.C., Sack, J.T., Yarov-Yarovoy, V., Kim, J. Il & Swartz, K.J. (2015) Tarantula toxins use common surfaces for interacting with Kv and ASIC ion channels. *eLife*, **4**, e06774. doi:10.7554/eLife.06774
Herrington, J., Zhou, Y.P., Bugianesi, R.M., Dulski, P.M., Feng, Y., Warren, V.A., Smith, M.M., Kohler, M.G., Garsky, V.M., Sanchez, M., Wagner, M., Raphaelli, K., Banerjee, P., Ahaghotu, C., Wunderler, D., Priest, B.T., Mehl, J.T., Garcia, M.L., *et al.* (2006) Blockers of the Delayed-Rectifier Potassium Current in Pancreatic Beta-Cells Enhance Glucose-Dependent Insulin Secretion. *Diabetes*, **55**, 1034–1042. doi:10.2337/diabetes.55.04.06.db05-0788
Hönigsperger, C., Nigro, M.J. & Storm, J.F. (2017) Physiological roles of Kv2 channels in entorhinal cortex layer II stellate cells revealed by Guangxitoxin-1E. *The Journal of Physiology*, **595**, 739–757. doi:10.1113/JP273024
Irannejad, R., Tomshine, J.C., Tomshine, J.R., Chevalier, M., Mahoney, J.P., Steyaert, J., Rasmussen, S.G.F., Sunahara, R.K., El-Samad, H., Huang, B. & Zastrow, M. von. (2013) Conformational biosensors reveal GPCR signalling from endosomes. *Nature*, **495**, 534–8. doi:10.1038/nature12000
Islas, L.D. & Sigworth, F.J. (1999) Voltage sensitivity and gating charge in Shaker and Shab family potassium channels. *The Journal of General Physiology*, **114**, 723–42. doi:10.1085/jgp.114.5.723
Jara-Oseguera, A., Ishida, I.G., Rangel-Yescas, G.E., Espinosa-Jalapa, N., Pérez-Guzmán, J.A., Elías-Viñas, D., Lagadec, R. Le, Rosenbaum, T. & Islas, L.D. (2011) Uncoupling charge movement from channel opening in voltage-gated potassium channels by ruthenium complexes. *The Journal of Biological Chemistry*, **286**, 16414–25. doi:10.1074/jbc.M110.198010
Johnson, B., Leek, A.N., Solé, L., Maverick, E.E., Levine, T.P. & Tamkun, M.M. (2018) Kv2 potassium channels form endoplasmic reticulum/plasma membrane junctions via interaction with VAPA and VAPB. *Proceedings of the National Academy of Sciences of the United States of America*, **115**, E7331–E7340. doi:10.1073/pnas.1805757115
Kaczmarek, L.K. (2006) Non-conducting functions of voltage-gated ion channels. *Nature Reviews Neuroscience*, **7**, 761–771, Nature Publishing Group. doi:10.1038/nrn1988
Kihira, Y., Hermanstyne, T.O. & Misonou, H. (2010) Formation of Heteromeric Kv2 Channels in Mammalian Brain Neurons. *Journal of Biological Chemistry*, **285**, 15048–15055. doi:10.1074/jbc.M109.074260
Kimm, T., Khaliq, Z.M. & Bean, B.P. (2015) Differential Regulation of Action Potential Shape and Burst-Frequency Firing by BK and Kv2 Channels in Substantia Nigra Dopaminergic Neurons. *The Journal of Neuroscience*, **35**, 16404–17. doi:10.1523/JNEUROSCI.5291-14.2015
Kirmiz, M., Gillies, T.E., Dickson, E.J. & Trimmer, J.S. (2019) Neuronal ER-plasma membrane junctions organized by Kv2-VAP pairing recruit Nir proteins and affect phosphoinositide

homeostasis. *The Journal of Biological Chemistry*, **294**, 17735–17757. doi:10.1074/jbc.RA119.007635

Kirmiz, Michael, Palacio, S., Thapa, P., King, A.N., Sack, J.T. & Trimmer, J.S. (2018) Remodeling neuronal ER-PM junctions is a conserved nonconducting function of Kv2 plasma membrane ion channels. *Molecular Biology of the Cell*, **29**, 2410–2432. doi:10.1091/mbc.E18-05-0337

Kirmiz, M., Vierra, N.C., Palacio, S. & Trimmer, J.S. (2018) Identification of VAPA and VAPB as Kv2 Channel-Interacting Proteins Defining Endoplasmic Reticulum–Plasma Membrane Junctions in Mammalian Brain Neurons. *The Journal of Neuroscience*, **38**, 7562–7584. doi:10.1523/JNEUROSCI.0893-18.2018

Kobrinsky, E., Stevens, L., Kazmi, Y., Wray, D. & Soldatov, N.M. (2006) Molecular rearrangements of the Kv2.1 potassium channel termini associated with voltage gating. *The Journal of Biological Chemistry*, **281**, 19233–40. doi:10.1074/jbc.M601231200

Lee, H.C., Wang, J.M. & Swartz, K.J. (2003) Interaction between extracellular Hanatoxin and the resting conformation of the voltage-sensor paddle in Kv channels. *Neuron*, **40**, 527–36. doi:10.1016/S0896-6273(03)00636-6

Lewis, G.N. (1925) A New Principle of Equilibrium. *Proceedings of the National Academy of Sciences of the United States of America*, **11**, 179–83. doi:10.1073/pnas.11.3.179

Li, H., Guo, W., Xu, H., Hood, R., Benedict, A.T. & Nerbonne, J.M. (2001) Functional expression of a GFP-tagged Kv1.5 alpha-subunit in mouse ventricle. *American Journal of Physiology. Heart and Circulatory Physiology*, **281**, H1955-67. doi:10.1152/ajpheart.2001.281.5.H1955

Lin, M.Z. & Schnitzer, M.J. (2016) Genetically encoded indicators of neuronal activity. *Nature Neuroscience*, **19**, 1142–1153. doi:10.1038/nn.4359

Liu, P.W. & Bean, B.P. (2014) Kv2 channel regulation of action potential repolarization and firing patterns in superior cervical ganglion neurons and hippocampal CA1 pyramidal neurons. *The Journal of Neuroscience*, **34**, 4991–5002. doi:10.1523/JNEUROSCI.1925-13.2014

Long, S.B., Campbell, E.B. & Mackinnon, R. (2005) Voltage Sensor of Kv1.2: Structural Basis of Electromechanical Coupling. *Science*, **309**, 903–908. doi:10.1126/science.1116270

Long, S.B., Tao, X., Campbell, E.B. & MacKinnon, R. (2007) Atomic structure of a voltage-dependent K+ channel in a lipid membrane-like environment. *Nature*, **450**, 376–82. doi:10.1038/nature06265

Maffie, J.K., Dvoretskova, E., Bougis, P.E., Martin-Eauclaire, M.-F. & Rudy, B. (2013) Dipeptidyl-peptidase-like-proteins confer high sensitivity to the scorpion toxin AmmTX3 to Kv4-mediated A-type K+ channels. *The Journal of Physiology*, **591**, 2419–27. doi:10.1113/jphysiol.2012.248831

Maletic-Savatic, M., Lenn, N.J. & Trimmer, J.S. (1995) Differential spatiotemporal expression of K+ channel polypeptides in rat hippocampal neurons developing in situ and in vitro. *The Journal of Neuroscience*, **15**, 3840–51.

Malin, S.A., Nerbonne, J.M. & Tamkun, M.M. (2013) Delayed Rectifier K+ Currents, IK, Are Encoded by Kv2 alpha -Subunits and Regulate Tonic Firing in Mammalian Sympathetic Neurons. *Journal of Neuroscience*, **22**, 10094–10105. doi:10.1523/jneurosci.3008-12.2013

McCord, M.C. & Aizenman, E. (2013) Convergent Ca2+ and Zn2+ signaling regulates apoptotic Kv2.1 K+ currents. *Proceedings of the National Academy of Sciences of the United States of America*, **110**, 13988–93. doi:10.1073/pnas.1306238110

McCormack, K., Santos, S., Chapman, M.L., Krafte, D.S., Marron, B.E., West, C.W., Krambis, M.J., Antonio, B.M., Zellmer, S.G., Printzenhoff, D., Padilla, K.M., Lin, Z., Wagoner, P.K., Swain, N.A., Stupple, P.A., Groot, M. de, Butt, R.P. & Castle, N.A. (2013) Voltage sensor interaction site for selective small molecule inhibitors of voltage-gated sodium channels. *Proceedings of the National Academy of Sciences of the United States of America*, **110**, E2724–E2732. doi:10.1073/pnas.1220844110

McDonough, S.I., Mintz, I.M. & Bean, B.P. (1997) Alteration of P-type calcium channel gating by the spider toxin omega-Aga-IVA. *Biophysical Journal*, **72**, 2117–28. doi:10.1016/S0006-3495(97)78854-4

Milescu, M., Bosmans, F., Lee, S., Alabi, A.A., Kim, J. Il & Swartz, K.J. (2009) Interactions between lipids and voltage sensor paddles detected with tarantula toxins. *Nature structural & molecular biology*, **16**, 1080–5. doi:10.1038/nsmb.1679

Misonou, H., Mohapatra, D.P., Park, E.W., Leung, V., Zhen, D., Misonou, K., Anderson, A.E. & Trimmer, J.S. (2004) Regulation of ion channel localization and phosphorylation by neuronal activity. *Nature Neuroscience*, **7**, 711–8. doi:10.1038/nn1260

Misonou, H., Mohapatra, D.P., Menegola, M. & Trimmer, J.S. (2005) Calcium- and metabolic state-dependent modulation of the voltage-dependent Kv2.1 channel regulates neuronal excitability in response to ischemia. *The Journal of Neuroscience*, **25**, 11184–93. doi:10.1523/JNEUROSCI.3370-05.2005

O'Connell, K.M.S., Loftus, R. & Tamkun, M.M. (2010) Localization-dependent activity of the Kv2.1 delayed-rectifier K+ channel. *Proceedings of the National Academy of Sciences of the United States of America*, **107**, 12351–6.doi:10.1073/pnas.1003028107

Opitz-Araya, X. & Barria, A. (2011) Organotypic hippocampal slice cultures. *Journal of Visualized Experiments*, MyJoVE Corporation. doi:10.3791/2462

Pal, S., Hartnett, K.A., Nerbonne, J.M., Levitan, E.S. & Aizenman, E. (2003) Mediation of neuronal apoptosis by Kv2.1-encoded potassium channels. *The Journal of Neuroscience*, **23**, 4798–802. doi: 10.1523/JNEUROSCI.23-12-04798.2003

Park, K.S., Mohapatra, D.P., Misonou, H. & Trimmer, J.S. (2006) Graded regulation of the Kv2.1 potassium channel by variable phosphorylation. *Science*, **313**, 976–9. doi:10.1126/science.1124254

Peltola, M.A., Kuja-Panula, J., Lauri, S.E., Taira, T. & Rauvala, H. (2011) AMIGO is an auxiliary subunit of the Kv2.1 potassium channel. *EMBO Reports*, **12**, 1293–1299. doi:10.1038/embor.2011.204

Peretz, A., Pell, L., Gofman, Y., Haitin, Y., Shamgar, L., Patrich, E., Kornilov, P., Gourgy-Hacohen, O., Ben-Tal, N. & Attali, B. (2010) Targeting the voltage sensor of Kv7.2 voltage-gated K+ channels with a new gating-modifier. *Proceedings of the National Academy of Sciences of the United States of America*, **107**, 15637–42. doi:10.1073/pnas.0911294107

Pologruto, T.A., Sabatini, B.L. & Svoboda, K. (2003) ScanImage: flexible software for operating laser scanning microscopes. *Biomedical Engineering Online*, **2**, 13. doi:10.1186/1475-925X-2-13

Sack, J.T., Aldrich, R.W. & Gilly, W.F. (2004) A gastropod toxin selectively slows early transitions in the Shaker K channel's activation pathway. *The Journal of General Physiology*, **123**, 685–96. doi:10.1085/jgp.200409047

Sack, J.T., Stephanopoulos, N., Austin, D.C., Francis, M.B. & Trimmer, J.S. (2013) Antibody-guided photoablation of voltage-gated potassium currents. *The Journal of General*

Physiology, **142**, 315–24. doi:10.1085/jgp.201311023
Schmalhofer, W.A., Calhoun, J., Burrows, R., Bailey, T., Kohler, M.G., Weinglass, A.B., Kaczorowski, G.J., Garcia, M.L., Koltzenburg, M. & Priest, B.T. (2008) ProTx-II, a selective inhibitor of NaV1.7 sodium channels, blocks action potential propagation in nociceptors. *Molecular Pharmacology*, **74**, 1476–84. doi:10.1124/mol.108.047670
Schneider, C.A., Rasband, W.S. & Eliceiri, K.W. (2012) NIH Image to ImageJ: 25 years of image analysis. *Nature Methods*, **9**, 671–5. doi:10.1038/nmeth.2089
Schneider, M.F. & Chandler, W.K. (1973) Voltage dependent charge movement of skeletal muscle: a possible step in excitation-contraction coupling. *Nature*, **242**, 244–6. doi:10.1038/242244a0
Scholle, A., Dugarmaa, S., Zimmer, T., Leonhardt, M., Koopmann, R., Engeland, B., Pongs, O. & Benndorf, K. (2004) Rate-limiting reactions determining different activation kinetics of Kv1.2 and Kv2.1 channels. *The Journal of Membrane Biology*, **198**, 103–12. doi:10.1007/s00232-004-0664-0
Seoh, S.A., Sigg, D., Papazian, D.M. & Bezanilla, F. (1996) Voltage-sensing residues in the S2 and S4 segments of the Shaker K+ channel. *Neuron*, **16**, 1159–67. doi:10.1016/S0896-6273(00)80142-7
Shi, G., Kleinklaus, A.K., Marrion, N. V & Trimmer, J.S. (1994) Properties of Kv2.1 K+ channels expressed in transfected mammalian cells. *The Journal of Biological Chemistry*, **269**, 23204–11.
Shi, G., Nakahira, K., Hammond, S., Rhodes, K.J., Schechter, L.E. & Trimmer, J.S. (1996) Beta subunits promote K+ channel surface expression through effects early in biosynthesis. *Neuron*, **16**, 843–52. doi:10.1016/S0896-6273(00)80104-X
Shibata, R., Misonou, H., Campomanes, C.R., Anderson, A.E., Schrader, L.A., Doliveira, L.C., Carroll, K.I., Sweatt, J.D., Rhodes, K.J. & Trimmer, J.S. (2003) A fundamental role for KChIPs in determining the molecular properties and trafficking of Kv4.2 potassium channels. *The Journal of Biological Chemistry*, **278**, 36445–54. doi:10.1074/jbc.M306142200
Shimony, E., Sun, T., Kolmakova-Partensky, L. & Miller, C. (1994) Engineering a uniquely reactive thiol into a cysteine-rich peptide. *Protein Engineering*, **7**, 503–7. doi:10.1093/protein/7.4.503
Singer-Lahat, D., Sheinin, A., Chikvashvili, D., Tsuk, S., Greitzer, D., Friedrich, R., Feinshreiber, L., Ashery, U., Benveniste, M., Levitan, E.S. & Lotan, I. (2007) K+ channel facilitation of exocytosis by dynamic interaction with syntaxin. *The Journal of Neuroscience*, **27**, 1651–8. doi:10.1523/JNEUROSCI.4006-06.2007
Speca, D.J., Ogata, G., Mandikian, D., Bishop, H.I., Wiler, S.W., Eum, K., Wenzel, H.J., Doisy, E.T., Matt, L., Campi, K.L., Golub, M.S., Nerbonne, J.M., Hell, J.W., Trainor, B.C., Sack, J.T., Schwartzkroin, P.A. & Trimmer, J.S. (2014) Deletion of the Kv2.1 delayed rectifier potassium channel leads to neuronal and behavioral hyperexcitability. *Genes, Brain and Behavior*, **13**, 394–408. doi:10.1111/gbb.12120
Stoppini, L., Buchs, P.A. & Muller, D. (1991) A simple method for organotypic cultures of nervous tissue. *Journal of Neuroscience Methods*, **37**, 173–82. doi:10.1016/0165-0270(91)90128-M
Swartz, K.J. (2007) Tarantula toxins interacting with voltage sensors in potassium channels. *Toxicon*, **49**, 213–30. doi:10.1016/j.toxicon.2006.09.024
Tao, X., Lee, A., Limapichat, W., Dougherty, D.A. & MacKinnon, R. (2010) A Gating Charge

Transfer Center in Voltage Sensors. *Science*, **328**, 67–73. doi:10.1126/science.1185954
Tilley, D.C., Angueyra, J.M., Eum, K.S., Kim, H., Chao, L.H., Peng, A.W. & Sack, J.T. (2019) The tarantula toxin GxTx detains K+ channel gating charges in their resting conformation. *The Journal of General Physiology*, **151**, 292–315. doi:10.1085/jgp.201812213
Tilley, D.C., Eum, K.S., Fletcher-Taylor, S., Austin, D.C., Dupre, C., Patron, L.A., Garcia, R.L., Lam, K., Yarov-Yarovoy, V., Cohen, B.E. & Sack, J.T. (2014) Chemoselective tarantula toxins report voltage activation of wild-type ion channels in live cells. *Proceedings of the National Academy of Sciences of the United States of America*, **111**, E4789-96. doi:10.1073/pnas.1406876111
Trapani, J.G. & Korn, S.J. (2003) Control of ion channel expression for patch clamp recordings using an inducible expression system in mammalian cell lines. *BMC Neuroscience*, **4**, 15. doi:10.1186/1471-2202-4-15
Trimmer, J.S. (1991) Immunological identification and characterization of a delayed rectifier K+ channel polypeptide in rat brain. *Proceedings of the National Academy of Sciences of the United States of America*, **88**, 10764–8. doi:10.1073/pnas.88.23.10764
Tsvetanova, N.G., Irannejad, R. & Zastrow, M. von. (2015) G Protein-coupled Receptor (GPCR) Signaling via Heterotrimeric G Proteins from Endosomes. *Journal of Biological Chemistry*, **290**, 6689–6696. doi:10.1074/jbc.R114.617951
Turner, M., Anderson, D., Nieves, M., Bartels, P., Coleman, A., Henderson, P., Man, K.N.M., Yarov-Yarovoy, V., Bers, D., Navedo, M., Horne, M., Ames, J.B. & Hell, J. (2019) α-Actinin-1 promotes activity of the L-type Ca2+ Channel Cav1.2. *EMBO (In Press)*.
Vacher, H., Mohapatra, D.P. & Trimmer, J.S. (2008) Localization and targeting of voltage-dependent ion channels in mammalian central neurons. *Physiological Reviews*, **88**, 1407–47. doi:10.1152/physrev.00002.2008
Vierra, N.C., Kirmiz, M., List, D. van der, Santana, L.F. & Trimmer, J.S. (2019) Kv2.1 mediates spatial and functional coupling of L-type calcium channels and ryanodine receptors in mammalian neurons. *eLife*, **8**. doi:10.7554/eLife.49953
Woods, G. & Zito, K. (2008) Preparation of gene gun bullets and biolistic transfection of neurons in slice culture. *Journal of Visualized Experiments*, pii:675. doi:10.3791/675
Xia, X.M., Ding, J.P. & Lingle, C.J. (1999) Molecular basis for the inactivation of Ca2+- and voltage-dependent BK channels in adrenal chromaffin cells and rat insulinoma tumor cells. *The Journal of Neuroscience*, **19**, 5255–64. doi:10.1523/jneurosci.19-13-05255.1999
Xu, H., Barry, D.M., Li, H., Brunet, S., Guo, W. & Nerbonne, J.M. (1999) Attenuation of the Slow Component of Delayed Rectification, Action Potential Prolongation, and Triggered Activity in Mice Expressing a Dominant-Negative Kv2 α Subunit. *Circulation Research*, **85**, 623–633. doi:10.1161/01.RES.85.7.623
Xu, Hui, Li, T., Rohou, A., Arthur, C.P., Tzakoniati, F., Wong, E., Estevez, A., Kugel, C., Franke, Y., Chen, J., Ciferri, C., Hackos, D.H., Koth, C.M. & Payandeh, J. (2019) Structural Basis of Nav1.7 Inhibition by a Gating-Modifier Spider Toxin. *Cell*, **176**, 1238–1239. doi:10.1016/j.cell.2019.01.047
Yang, F. & Zheng, J. (2014) High temperature sensitivity is intrinsic to voltage-gated potassium channels. *eLife*, **3**, e03255. doi:10.7554/eLife.03255
Yang, W. & Yuste, R. (2017) In vivo imaging of neural activity. *Nature Methods*, **14**, 349–359. doi:10.1038/nmeth.4230
Zagotta, W.N., Hoshi, T., Dittman, J. & Aldrich, R.W. (1994) Shaker potassium channel gating. II: Transitions in the activation pathway. *The Journal of General Physiology*, **103**, 279–319.

doi:10.1085/jgp.103.2.279
Zhang, A.H., Sharma, G., Undheim, E.A.B., Jia, X. & Mobli, M. (2018) A complicated complex: Ion channels, voltage sensing, cell membranes and peptide inhibitors. *Neuroscience Letters*, **679**, 35–47. doi:10.1016/j.neulet.2018.04.030
Zhang, G., Zheng, S., Liu, H. & Chen, P.R. (2015) Illuminating biological processes through site-specific protein labeling. *Chemical Society Reviews*, **44**, 3405–3417. doi:10.1039/C4CS00393D
Zito, K., Knott, G., Shepherd, G.M.G., Shenolikar, S. & Svoboda, K. (2004) Induction of Spine Growth and Synapse Formation by Regulation of the Spine Actin Cytoskeleton. *Neuron*, **44**, 321–334. doi:10.1016/j.neuron.2004.09.022

Figure Legends

Figure 1: ***GxTX-594 colocalizes with Kv2-GFP.***

A. Fluorescence from CHO cells transfected with Kv2.1-GFP (Top) or Kv2.2-GFP (Bottom) and labeled with GxTX-594. Optical sections were near the glass-adhered cell surface. Cells were incubated with 100 nM GxTX-594 for 5 minutes and rinsed before imaging. Fluorescence shown corresponds to emission of GFP (Left), Alexa Fluor 594 (Middle), or an overlay of GFP and Alexa Fluor 594 (Right). Scale bars are 20 µm.
B. Pearson correlation coefficient for GxTX-594 colocalization with Kv2.1-GFP or Kv2.2-GFP.
C. Ratio of magenta to green intensity between GxTX-594 and Kv2-GFP. Circles indicate measurements from individual cells. In panels B and C, pixel intensities were background subtracted before analyses by subtracting the average fluorescence of a background ROI that did not contain cells, from the ROI containing the cell. All data from the same application of GxTX-594. Bars are arithmetic mean.

Figure 1 Supplement 1: ***Synthesis of GxTX-594.***

A. Molecular model of GxTX-594. Scale bar is 10 angstroms.
B. HPLC chromatogram of Ser13Cys GxTX. Gradient described in *Methods* Ser13Cys GxTX eluted at 12.6 minutes, peak 1, which corresponds to 33% acetonitrile. MALDI-TOF MS profile of peak 1 (Inset). Rel. Int. is Relative Intensity.
C. HPLC chromatogram of GxTX-594 conjugation reaction between Alexa Fluor 594-maleimide and Ser13Cys GxTX. Peak 1 is Ser13Cys GxTX (Retention time: 12.8 minutes, 33% acetonitrile), peak 2 is a minor product from conjugation, and peak 3 is GxTX-594, the major product from conjugation (Retention time: 16.4 minutes, 35% acetonitrile). The fractions corresponding to peak 3 were combined.
D. HPLC chromatogram of the combined peak 3 fractions from panel C, a GxTX-594 preparation used in this study. 2 μL of 13.1 μM GxTX-594 diluted in 200 μL of 0.1 % TFA was injected. MALDI-TOF MS profile of the combined peak 3 fractions (Inset).

Figure 2: ***GxTX594 binds Kv2.1 in the presence of its auxiliary subunit AMIGO-1.***

A. Fluorescence from Kv2.1-CHO cells, some of which have been transfected with AMIGO-1-YFP. Imaging plane was near the glass-adhered cell surface. Cells were incubated in indicated concentrations of GxTX-594 for 15 minutes then washed out before imaging. Fluorescence shown corresponds to YFP (Green) and Alexa Fluor 594 (Magenta). Scale bar is 20 µm. Green line surrounds a representative AMIGO-1 positive ROI. Blue line surrounds an AMIGO-1 negative ROI.
B. Pearson correlation coefficient between AMIGO-1-YFP and GxTX-594 within AMIGO positive ROIs. Coefficients from 1000 nM dose of GxTX-594. n = 8 ROIs total over 3 independent experiments. Bar is arithmetic mean.
C. Time-lapse GxTX-594 fluorescence intensity from the dose-response experiment shown in A. The green trace represents the AMIGO-1-YFP positive ROI, the blue trace represents the AMIGO-1-YFP negative ROI. Fluorescence was not background-subtracted. F_{max} is intensity while cells were incubated in 1000 nM GxTX-594.
D. Changes in fluorescence were analyzed at each concentration from multiple dose response experiments. Hollow markers correspond to 3 independent experiments. Green represents AMIGO-1-YFP positive ROIs, blue represents AMIGO-1-YFP negative ROIs. Lines are fits of a Langmuir isotherm (Hill equation with slope held at 1) to obtain a dissociation constant (K_d) for GxTX-594; AMIGO-1-YFP positive K_d = 26.7 nM ± 14.3; AMIGO-1-YFP negative K_d = 26.9 nM ± 8.3.

Figure 3: ***GxTX-594 labeling responds to transmembrane voltage.***

A. Fluorescence intensities from an optical section of a voltage-clamped Kv2.1- CHO cell in 9 nM GxTX-594. Pseudocolored images indicate maximal intensities in white. Rows indicate voltage step taken from a holding potential of -80 mV. Columns indicate time after voltage step. Scale bar is 10 µm.

B. GxTX-594 fluorescence during steps to indicated voltages. Smooth lines are fits of monoexponential (Eq. 1): -40 mV $k_{\Delta F}$ = 2.2 x 10^{-2} ± 2.2 x 10^{-3} s^{-1}: 0 mV $k_{\Delta F}$ = 1.3 x 10^{-1} ± 2.3 x 10^{-3} s^{-1}, 40 mV $k_{\Delta F}$ = 2.6 x 10^{-1} ± 6.2 x 10^{-3} s^{-1} and 80 mV $k_{\Delta F}$ = 5.3 x 10^{-1} ± 1.1 x 10^{-2} s^{-1}. ROIs were hand-drawn around the apparent cell surface membrane based on GxTX-594 fluorescence. Background for subtraction was the average intensity of a region that did not contain cells over the time course of the voltage protocol. Each trace was normalized to initial fluorescence intensity before the application of the voltage stimulus.

C. Fluorescence intensity remaining at the end of 50 s steps to +80 mV. Each circle represents one cell. Background subtraction and normalization as in panel B.

D. Voltage-dependence of fluorescence intensity at the end of 50 s steps. Data normalized to 100% for -80 mV and 0% for +80 mV. Circle coloring indicates data from the same cell. Gray circles represent data shown in B. Black line is fit of a first-order Boltzmann equation as in Tilley et al., 2019: $V_{1/2}$ = -27.4 ± 2.5 mV, z = -1.38 ± 0.13 e_0. Blue line is prediction from Scheme I at 9 nM GxTX. Bars are arithmetic mean ± standard error.

E. Voltage dependence of fluorescence intensity kinetics at end of 50 s steps. Circle coloring is the same as panel D. Black line is a first-order Boltzmann equation fit to the logarithm of $k_{\Delta F}$: $V_{1/2}$ = 2.3 ± 7.9 mV, z = -1.14 ± 0.38 e_0. Blue line is prediction from Scheme I at 9 nM GxTX. Bars are geometric mean ± standard error.

Figure 3 Supplement 1: ***Spatial dependence of GxTX-594 labeling kinetics at the glass-adhered surface.***

We conducted experiments to determine the region of voltage-clamped cells from which to quantify dynamic fluorescence. The confocal imaging plane containing the most GxTX-594 fluorescence was the glass-adhered basal surface. We noticed that GxTX-594 fluorescence in the center of the basal surface appeared to respond more slowly to voltage changes than the periphery. To quantify this observation, concentric ROIs were drawn in the center of the basal surface of the cell and their average fluorescence intensities were compared to each other and an ROI at the cell periphery. In response to voltage change, the kinetics of fluorescence change were slower at the center of the basal surface and faster towards the outer periphery. We quantified rates of fluorescence change ($k_{\Delta F}$) by fitting a monoexponential function (Eq 1). $k_{\Delta F}$ progressively slowed as the ROI contracted from the perimeter of the cell. This difference in kinetics suggests that the concentration of freely diffusing GxTX-594 in the restricted space between the cell membrane and the glass surface is transiently non-uniform after voltage change. The location dependence of $k_{\Delta F}$ was more pronounced during GxTX-594 labeling at -80 mV than unlabeling at +40 mV. We suspect that the more extreme location dependence at -80 mV is due to a high density of Kv2.1 binding sites in the restricted extracellular space between the cell membrane and glass coverslip, such that GxTX-594 is depleted from solution by binding Kv2.1 before reaching the center of the cell. After unbinding at +40 mV, each GxTX-594 molecule is expected to be less likely to rebind to Kv2.1 proteins as it diffuses out from under the cell, because Kv2.1 voltage sensors are in an activated, low affinity conformation (Tilley *et al.* 2014, 2019). This expected difference in GxTX-594 buffering by Kv2.1 could explain the difference in location dependence of $k_{\Delta F}$ during labeling at -80 mV and unlabeling at +40 mV. To avoid complications resulting from the spatial variability of kinetics at the basal surface, further voltage-dependent labeling experiments were conducted while imaging at a plane above the coverslip, where the cell surface has unrestricted access to the extracellular solution.

A. Time lapse airy disk images of the glass-adhered surface of a voltage-clamped Kv2.1-CHO cell in 9 nM GxTX-594. Time index is in the upper left of each panel and membrane potential is indicated in the upper right. Scale bar in lower right of last panel is 10 μm

B. Airy disk image of the glass adhered surface of a voltage-clamped Kv2.1-CHO cell in 9 nM GxTX-594. Grey lines indicate boundaries of ROIs. ROI 1, 2, and 3 are concentric circles each with a respective diameter of 1.8, 4.9, and 9.1 µm. ROI 4 was hand-drawn to contain the apparent cell surface. In all cells analyzed, ROI 1-3 were concentric circles of the same sizes, while ROI 4 varied based on cell shape. Scale bar is 10 µm.

C. Representative traces of GxTX-594 fluorescence intensity response to voltage changes. Red lines are monoexponential fits (Eq. 1): 40 mV step ROI 1 $k_{\Delta F} = 4.3 \times 10^{-2} \pm 2.6 \times 10^{-3}$ s^{-1}, ROI 2 $k_{\Delta F} = 4.4 \times 10^{-2} \pm 1.6 \times 10^{-3}$ s^{-1}, ROI 3 $k_{\Delta F} = 5.7 \times 10^{-2} \pm 1.5 \times 10^{-3}$ s^{-1}, ROI 4 $k_{\Delta F} = 9.7 \times 10^{-2} \pm 3.3 \times 10^{-3}$ s^{-1}. -80 mV step ROI 1 $k_{\Delta F} = 4.3 \times 10^{-4} \pm 1.1 \times 10^{-5}$ s^{-1}, ROI 2 $k_{\Delta F} = 7.9 \times 10^{-4} \pm 5.3 \times 10^{-6}$ s^{-1}, ROI 3 $k_{\Delta F} = 2.8 \times 10^{-3} \pm 7.4 \times 10^{-6}$ s^{-1}, and ROI 4 $k_{\Delta F} = 5.5 \times 10^{-3} \pm 1.3 \times 10^{-4}$ s^{-1}. Background for subtraction was the average intensity of a region that did not contain cells over the time course of the voltage protocol. Each trace was normalized to initial fluorescence intensity before the application of the voltage stimulus.

D. Circles indicate $k_{\Delta F}$ at 40 mV from individual cells. Circle coloring indicates data from the same cell.

E. Circles indicate $k_{\Delta F}$ at -80 mV from individual cells. Circle coloring indicates data from the same cell.

Figure 3 Supplement 2: ***Temperature dependence of GxTX-594 on Kv2.1 CHO cells.***
To assess the temperature dependence of GxTX-594 labeling, the cell bath solution was held at either 27°C or 37°C and stepped to 0 mV for a measurement of $k_{\Delta F}$. The fold change in $k_{\Delta F}$ over this 10 °C difference, or Q_{10}, was 3.8-fold. This Q_{10} predicts a 1.3-fold increase in $k_{\Delta F}$ between 27 and 29°C, the temperature range of expreiments reported in Fig 3 E. This 1.3-fold increase was less than cell-to-cell variability observed.

A. Representative traces of GxTX-594 fluorescence intensity response to voltage changes at 27 °C (black) and 37 °C (gray). Smooth lines are fits of a monoexponential function (Eq. 1): 27 °C $k_{\Delta F} = 2.8 \times 10^{-2} \pm 3.9 \times 10^{-3}$ s^{-1}; 37 °C $k_{\Delta F} = 7.5 \times 10^{-2} \pm 5.4 \times 10^{-3}$ s^{-1}. Background was determined by taking the average fluorescence of a region that did not contain cells over the time course of the voltage protocol. This average was subtracted from each experimental group. Traces were normalized to initial fluorescence intensity before the application of the voltage stimulus.
B. $k_{\Delta F}$ at 27 °C and 37 °C. The rate of fluorescence change was significantly faster at higher temperatures (Mann-Whitney p = 0.0005). From geometric means (Bars), a Q_{10} of 3.8 was calculated between 27 °C and 37 °C. Each circle represents one cell, n = 7 both groups.

Figure 4: ***Frequency dependence of GxTX-594 response***

A. Fluorescence intensity on Kv2.1-expressing CHO cells incubated in 9 nM GxTX-594. GxTX-594 fluorescence before (Left), after 50 s of 200 Hz stimulus (Middle), and 100 s after the cell is returned to resting potential of -80 mV (Right). Note that in each panel the unpatched cell (Left cell in each panel) does not show a change in fluorescence. Scale bar is 10 µm. Patched cell is indicated by a white arrow.

B. Representative trace of GxTX-594 unlabeling at 200 Hz. The trace was fit using a monoexponential (Eq. 1). Fit is overlaid and is in red. The $k_{\Delta F}$ at 200 Hz was obtained from this fit. For 200 Hz $k_{\Delta F} = 2.23 \times 10^{-1} \pm 9.9 \times 10^{-3}$ s^{-1}. ROIs were hand drawn capturing the cell membrane based on GxTX-594 fluorescence such that only the cell membrane was selected without selecting the dark intracellular region. Background was determined by taking the average fluorescence of a region that did not contain cells over the time course of the protocol. This average was subtracted from each experimental group. F_{init} is the initial fluorescence intensity before the application of the frequency stimulus.

C. Decrease in fluorescence with increasing stimulus frequency. Circles indicate F/F_{init} from individual cells when stepped to +40 mV at indicated frequencies from a holding potential of -80 mV. Data normalized to 100% for -80 mV before frequency pulse. Circle coloring indicates data from the same cell. Black line is fit of a first-order Boltzmann equation as in Tilley et al., 2019: $V_{1/2} = -0.35 \pm 0.03$ mV, $z = 51.23 \pm 5.19$ e_0. Blue line represents decreases in fluorescence at increasing voltages derived from the model shown in Scheme I at a concentration of 9 nM. Bars are arithmetic mean ± standard error.

D. Increases in $k_{\Delta F}$ with increasing stimulus frequency. Rates were obtained from fitting decreases in fluorescence with a monoexponential (Eq. 1) as shown in B. Blue line represents the rates of fluorescence change at increasing frequencies derived from the model shown in Scheme I at a concentration of 9 nM. Bars are geometric mean ± standard error.

Figure 5: ***Relationship of GxTX-594 labeling to probability of Kv2 voltage sensor activation.***

A. Scheme I model predictions of concentration- and voltage-dependence of cell surface fluorescence intensity. Bottom axis represents membrane voltage while the top axis represents the ratio of activated to resting voltage sensors for unlabeled Kv2.1. Dashed black line represents the probability that voltage sensors of unlabeled Kv2.1 are in their resting conformation.

B. Scheme I model predictions of concentration- and voltage-dependence of $k_{\Delta F}$. Colors correspond to panel A.

Figure 6: ***GxTX-594 is selective for Kv2 proteins.***

A. Fluorescence from live CHO cells transfected with Kv2.1-GFP, Kv2.2-GFP, Kv4.2-GFP + KChIP2, Kv1.5-GFP + Kvβ2, or BK-GFP (Indicated by row) and labeled with GxTX-594. Airy disk imaging was from a plane above the glass-adhered surface. Cells were incubated with 100 nM GxTX-594 and 5 μg/mL WGA-405 then rinsed before imaging. Fluorescence shown corresponds to emission of GFP (Column 1), Alexa Fluor 594 (Column 2), WGA-405 (Column 3), or an overlay of GFP, Alexa Fluor 594, and WGA-405 (Column 4). Scale bars are 20 μm.

B. GxTX-594:GFP fluorescence intensity ratios for different K^+ channel-GFP types. F_{init} is the average GxTX-594:Kv2.1-GFP ratio. Circles indicate measurements from individual cells. Only cells with obvious GFP expression were analyzed. For analysis ROIs were drawn around the cell membrane indicated by WGA-405 fluorescence. Pixel intensities were background-subtracted before analyses by subtracting the average fluorescence of a background ROI that did not contain cells from the ROI containing the cell; this occasionally resulted in ROIs with negative intensity. Kv2.1 n = 16, Kv2.2 n = 10, Kv4.2 n = 13, Kv1.5 n = 13, BK n =10; n indicates the number of individual cells analyzed during a single application of GxTX-594. Bars are arithmetic mean. Significant differences were observed between GxTX:GFP ratio for Kv2.1 or Kv2.2 and Kv1.5, Kv4.2, or BK by Mann-Whitney ($p<0.0001$).

C. Pearson correlation coefficients between GxTX-594 and GFP. Same cells as panel B. Significant differences were observed between correlation coefficients for Kv2.1 or Kv2.2 and Kv1.5, Kv4.2, or BK by Mann-Whitney ($p<0.0001$).

Figure 6 Supplement 1: ***GFP-tagged K^+ channels exhibit expected outward currents.***

A. Exemplar whole-cell voltage clamp recordings of CHO cells expressing Kv2.1-GFP, Kv2.2-GFP, Kv4.2-GFP, Kv1.5-GFP, or BK-GFP. Recordings shown are representative responses to 100 ms steps from -100 mV to -40, 0 and +40 mV.
B. Fluorescence from live CHO cells transfected with Kv2.1-GFP, Kv2.2-GFP, Kv4.2-GFP Kv1.5-GFP, or BK-GFP (Indicated by row) and labeled with GxTX-594. Confocal imaging plane was above the glass-adhered surface. Cells were incubated with 100 nM GxTX-594 and 5 μg/mL WGA-405 and rinsed before imaging. Fluorescence shown corresponds to emission of GFP (Column 1), Alexa Fluor 594 (Column 2), WGA-405 (Column 3), or an overlay of GFP, Alexa Fluor 594, and WGA-405 (Column 4). Scale bars are 20 μm.
C. Background-subtracted GxTX-594:GFP ratio for different GFP and K^+ channel subtypes normalized to the average GxTX-594:Kv2.1-GFP ratio. Analysis same as in Figure 6 B. Kv2.1 n = 11, Kv2.2 n = 9, Kv4.2 n = 13, Kv1.5 = 13, and BK n =12. Cells were compiled from two independent GxTX-594 applications, each circle corresponds to a cell. Significant differences were observed between GxTX:GFP ratio for Kv2.1 or Kv2.2 and Kv1.5, Kv4.2, or BK by Mann-Whitney ($p<0.0001$).
D. Pearson correlation coefficients between GxTX-594 and GFP. Unless otherwise noted analysis was same as in Figure 6 C. Same cells as panel C.

Figure 7: **GxTX-594 labels CA1 hippocampal pyramidal neurons transfected with Kv2.1-GFP.**

A. Two-photon excitation images of fluorescence from the soma and proximal dendrites of a rat CA1 hippocampal pyramidal neuron in a brain slice six days after transfection with Kv2.1-GFP (Left), labeled with 100 nM GxTX-594 (Middle) and overlay (Right). Image represents a z-projection of 20 optical sections. Scale bar 10 µm.
B. A single optical section of the two-photon excitation image shown in A. GxTX-594 labels both Kv2.1-GFP puncta from a transfected cell and apparent endogenous Kv2 proteins from an untransfected cell in the same cultured slice (Right, arrow).
C. Pearson correlation coefficients from CA1 hippocampal neurons two, four, and six days after transfection with Kv2.1-GFP. Each circle represents a different neuron. Bars are arithmetic means.

Figure 7 Supplement 1: **GxTX-594 labels CA1 hippocampal pyramidal neurons transfected with Kv2.1-GFP.**

Two-photon excitation images rat CA1 hippocampal pyramidal neurons in brain slices as in Figure 7 A. Kv2.1-GFP (Left), GxTX-594 (Middle) and overlay (Right). Scale bars 10 μm.

A. Two days after transfection with Kv2.1-GFP.
B. Four days after transfection with Kv2.1-GFP.
C. Six days after transfection with Kv2.1-GFP.

Figure 8: **GxTX-594 puncta on hippocampal CA1 neurons are sensitive to voltage stimulus**

A. Single two-photon excitation optical section of fluorescence from CA1 pyramidal neurons in a cultured hippocampal slice after incubation with 100 nM GxTX-594. Scale bar is 5 µm.
B. GxTX-594 fluorescence from a single two-photon excitation optical section before and during depolarization of a whole cell patch-clamped neuron. Text labels of holding potential (-70 mV or 0 mV) indicate approximate position of the patch-clamp pipette. Red arrows indicate stimulus-sensitive puncta, white arrows indicate stimulus-insensitive puncta. Left panel is the average fluorescence of the three frames at -70 mV before depolarization while the right panel is the average fluorescence of three frames after holding potential was stepped to 0 mV. Scale bar is 5 µm. Supplementary Movie 1 contains time-lapse images from this experiment.
C. ROIs used in analysis for panels D, E, and F. Same slice as panel B. ROI 1 contains the apparent plasma membrane of the cell body of the patch-clamped neuron, it was generated by drawing a path tracing the apparent plasma membrane and then expanding to an ROI containing 15 pixels on either side of the path (1.2 µm total width). ROI 2 contains the area 15-45 pixels outside the membrane path (1.2 µm total width). RO1 3 contains the area more than 45 pixels outside of the membrane path. ROI 0 contains the area more than 15 pixels inside the membrane path. Scale bar is 5 µm.
D. Fluorescence from each ROI shown in C. Squares represent ROI 0, circles represent ROI 1, upward triangles represent ROI 2 and upside-down triangles represent ROI 3. Background was defined as the mean fluorescence of ROI 0 during the experiment. F_{init} was defined as the mean fluorescence of ROI 1 during the first six frames, after subtraction of background. Dotted lines represent the average fluorescence of the first six frames of each ROI. The voltage protocol is shown above.
E. Change in fluorescence during a 0 mV step for different ROIs in multiple hippocampal slices. ROIs for each slice were defined by methods described in panel C. Circles represent mean fluorescence from six frames during 0 mV stimulus (F), normalized to mean fluorescence from same ROI in six frames before stimulus (F_{init}). Circle color is consistent between ROIs for each hippocampal slice, red circles are from the slice shown in panel D. Black bars are arithmetic mean ± standard error from 3 hippocampal slices.

F. Kinetics of fluorescence change from ROI 1 during a 0 mV step in multiple hippocampal slices. ROI 1 for each slice was defined by the method described in panel C. Lines are monoexponential fits (Eq.1). $k_{\Delta F}$ = 6.8 x 10^{-2} ± 2.6 x 10^{-2} s^{-1} (yellow), 6.8 x 10^{-2} ± 4.6 x 10^{-2} s^{-1} (red), and 4.9 x 10^{-2} ± 2.1 x 10^{-2} s^{-1} (green). The voltage protocol is shown above. Colors of individual circles indicate the same slices as panel E.

G. Region of interest used in analysis for panels H, I, and J. Same image as panel C. The shaded ROI was generated by drawing a path tracing the apparent plasma membrane and then expanding to an ROI containing 5 pixels on either side of the path (0.4 µm total width). Numbers indicate puncta that appear as peaks in panel H. Scale bar is 5 µm.

H. A plot of the fluorescence intensity along the ROI shown in panel G before (red trace) and during (black trace) 0 mV stimulus. Numbers above peaks correspond to puncta labeled in panel G. Red trace: mean fluorescence intensity during the three frames immediately before the stimulus, normalized to mean intensity of entire ROI (black dotted line), plotted against distance along path. Black trace: mean fluorescence intensity during three frames at 0 mV, normalized by the same F_{init} value as the red trace.

I. Kinetics of fluorescence change of individual puncta from panel G. Puncta intensity are average intensity of points extending to half maxima of each peak in panel H. Asterisks indicate mean fluorescence intensity of puncta 1 (pink), 4 (red), and 5 (dark red). Lines are monoexponential fits (Eq.1). $k_{\Delta F}$ = 7.1 x 10^{-2} ± 2.9 x 10^{-2} s^{-1} (pink), 6.7 x 10^{-2} ± 2.5 x 10^{-2} s^{-1} (red) and 1.2 x 10^{-1} ± 5.6 x 10^{-2} s^{-1} (dark red). Fits to other puncta had standard deviations larger than $k_{\Delta F}$ values, and were excluded. F_{init} was defined as the mean background subtracted fluorescence of the puncta during the six frames before stimuli. The voltage protocol is displayed above. Blue line is prediction from Scheme I.

J. Comparison of fluorescence change of puncta and inter-puncta regions in response to 0 mV stimulus. The regions before stimulus shown in the red line of panel H that had $F/F_{init} \geq 1$ (above average) were binned separately from regions with $F/F_{init} < 1$. The mean fluorescence of each region during 0 mV stimulus (panel H black trace) was compared to the fluorescence before stimulus (panel H red trace). Circles indicate values from three independent hippocampal slices, colors indicate same slices as panel E and F. Black bars are arithmetic mean ± standard error.

K. Rate of fluorescence change of GxTX-594 after a 0 mV stimulus; from puncta (as in panel I), ROI 1 (as in panel F) or Kv2.1-CHO cells in 100 nM GxTX-594. Kv2.1-CHO cells were imaged at the same temperature as neurons (30 °C) using neuronal intracellular solution. Normal CHO extracellular solution (CE) was used for Kv2.1-CHO cell experiments. Kv2.1-CHO measurements were made by airy disk confocal imaging. Black bars are mean ± SEM from data shown. Dashed blue line is $k_{\Delta F} = 6.31 \times 10^{-2}\ s^{-1}$ prediction of Scheme I.

Table 1

Parameters used for calculations with Scheme I Model

Parameter	Value
$k_{on,resting}$	0.30 μM^{-1} s^{-1}
$k_{off,resting}$	0.0081 s^{-1}
$k_{on,activated}$	0.21 $\mu M^{-1} s^{-1}$
$k_{off,activated}$	0.39 s^{-1}
$V_{1/2,unlabeled}$	-32 mV
$V_{1/2,labeled}$	41 mV
z	1.5 e_0

Figure 1

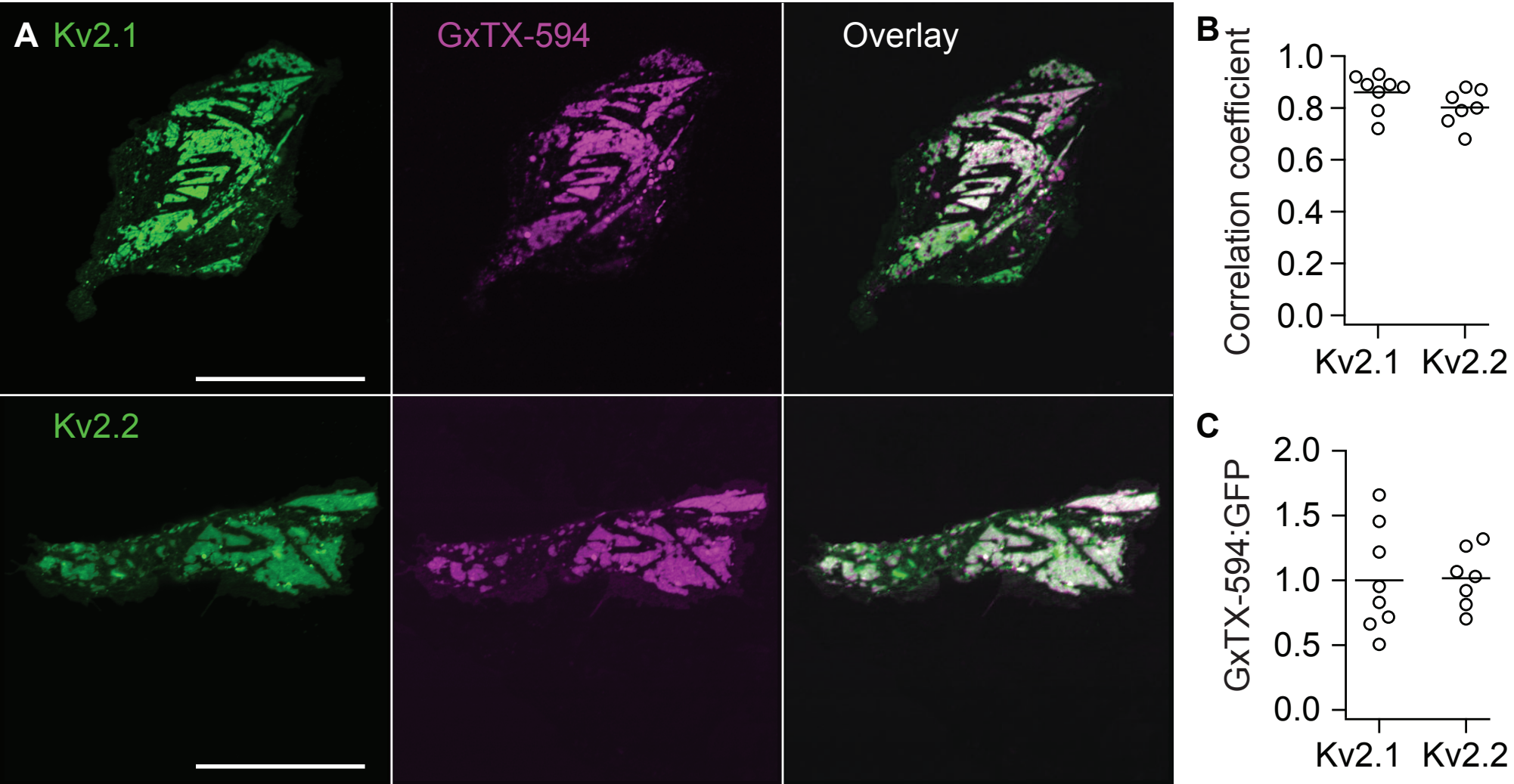
A
Kv2.1
GxTX-594
Overlay
Kv2.2
B
Correlation coefficient
1.0
0.8
0.6
0.4
0.2
0.0
Kv2.1
Kv2.2
C
GxTX-594:GFP
2.0
1.5
1.0
0.5
0.0
Kv2.1
Kv2.2

Figure 1 Supplement 1

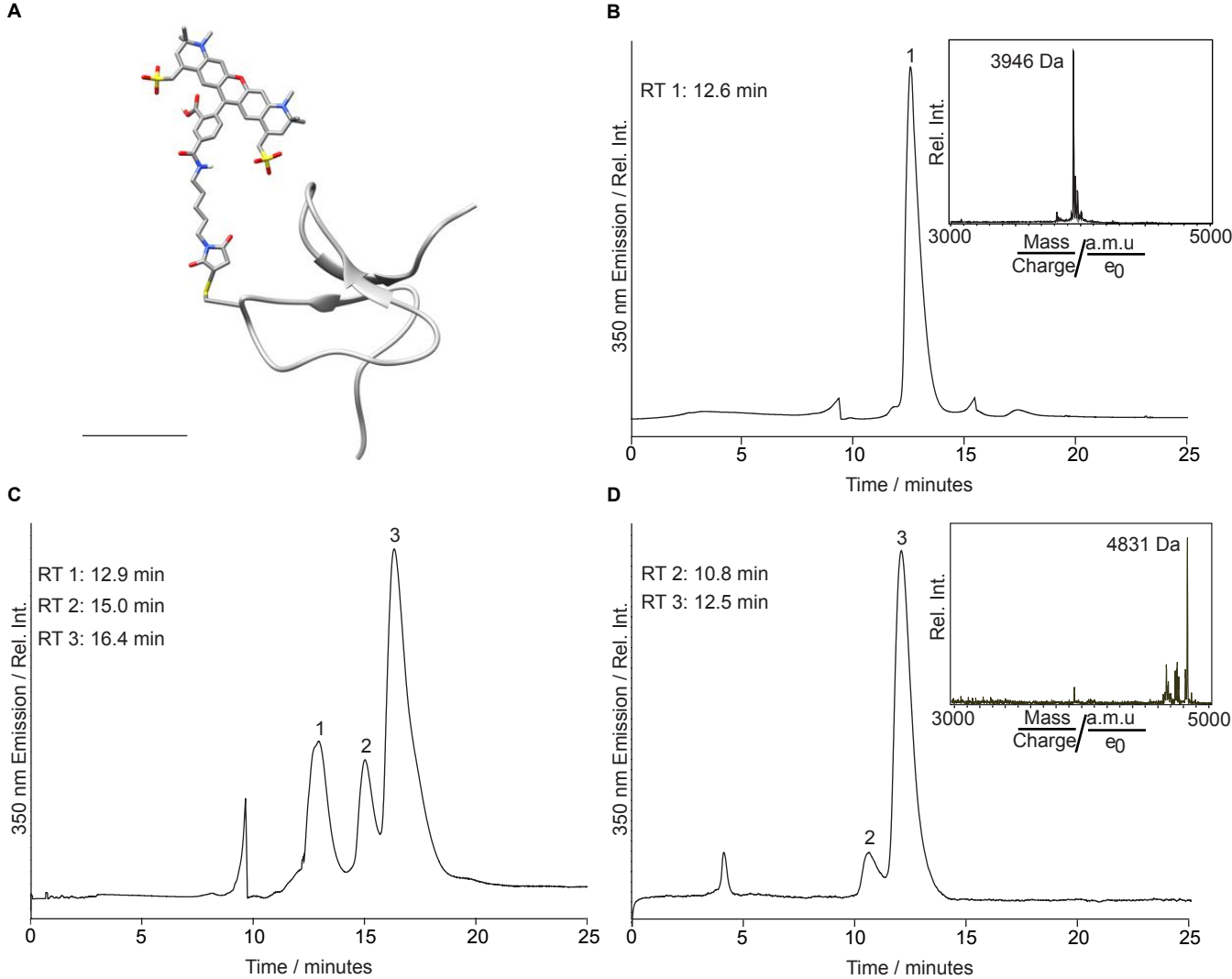

Figure 2

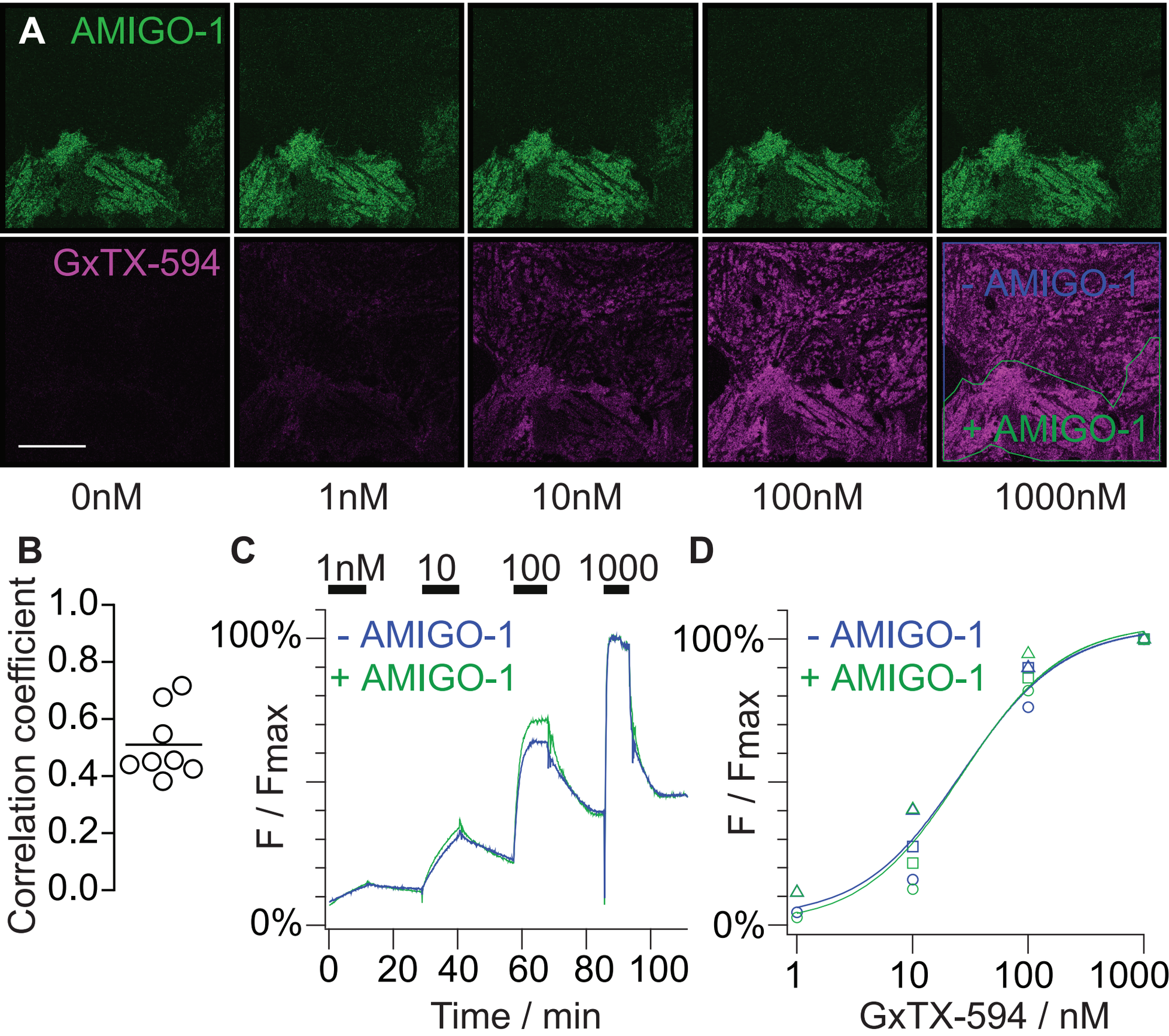
A
AMIGO-1
GxTX-594
- AMIGO-1
+ AMIGO-1
0nM
1nM
10nM
100nM
1000nM
B
Correlation coefficient
1.0
0.8
0.6
0.4
0.2
0.0
C
1nM
10
100
1000
100%
0%
F / Fmax
- AMIGO-1
+ AMIGO-1
0
20
40
60
80
100
Time / min
D
100%
0%
F / Fmax
- AMIGO-1
+ AMIGO-1
1
10
100
1000
GxTX-594 / nM

Figure 3

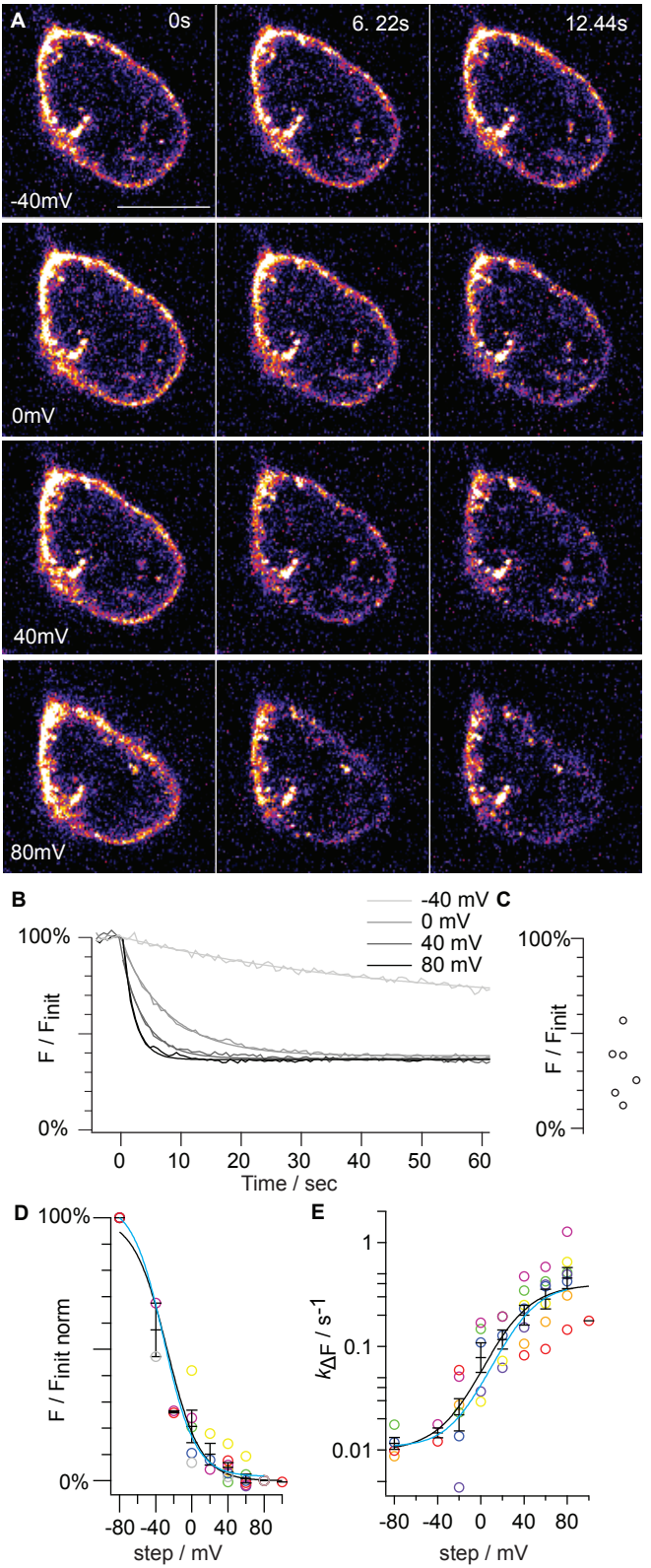
A
0s
6. 22s
12.44s
-40mV
0mV
40mV
80mV
B
-40 mV
0 mV
40 mV
80 mV
100%
0%
F / F_init
0
10
20
30
40
50
60
Time / sec
C
100%
0%
F / F_init
D
100%
0%
F / F_init norm
-80
-40
0
40
80
step / mV
E
1
0.1
0.01
k_ΔF / s^-1
-80
-40
0
40
80
step / mV

Figure 3 Supplement 1

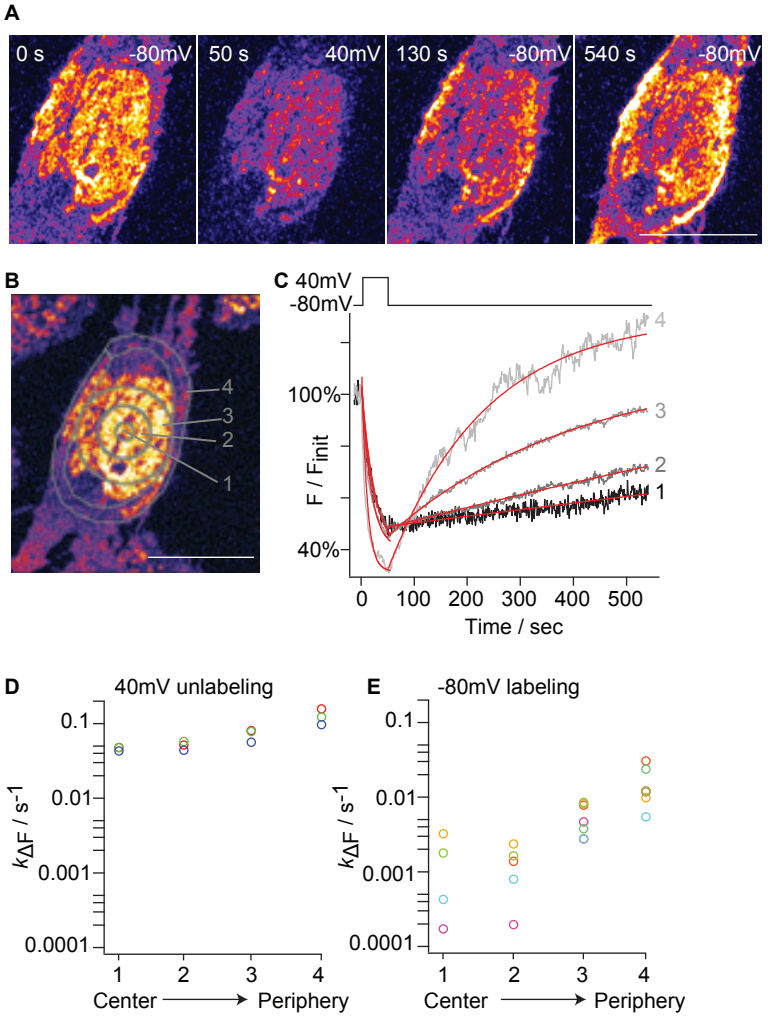

Figure 3 Supplement 2

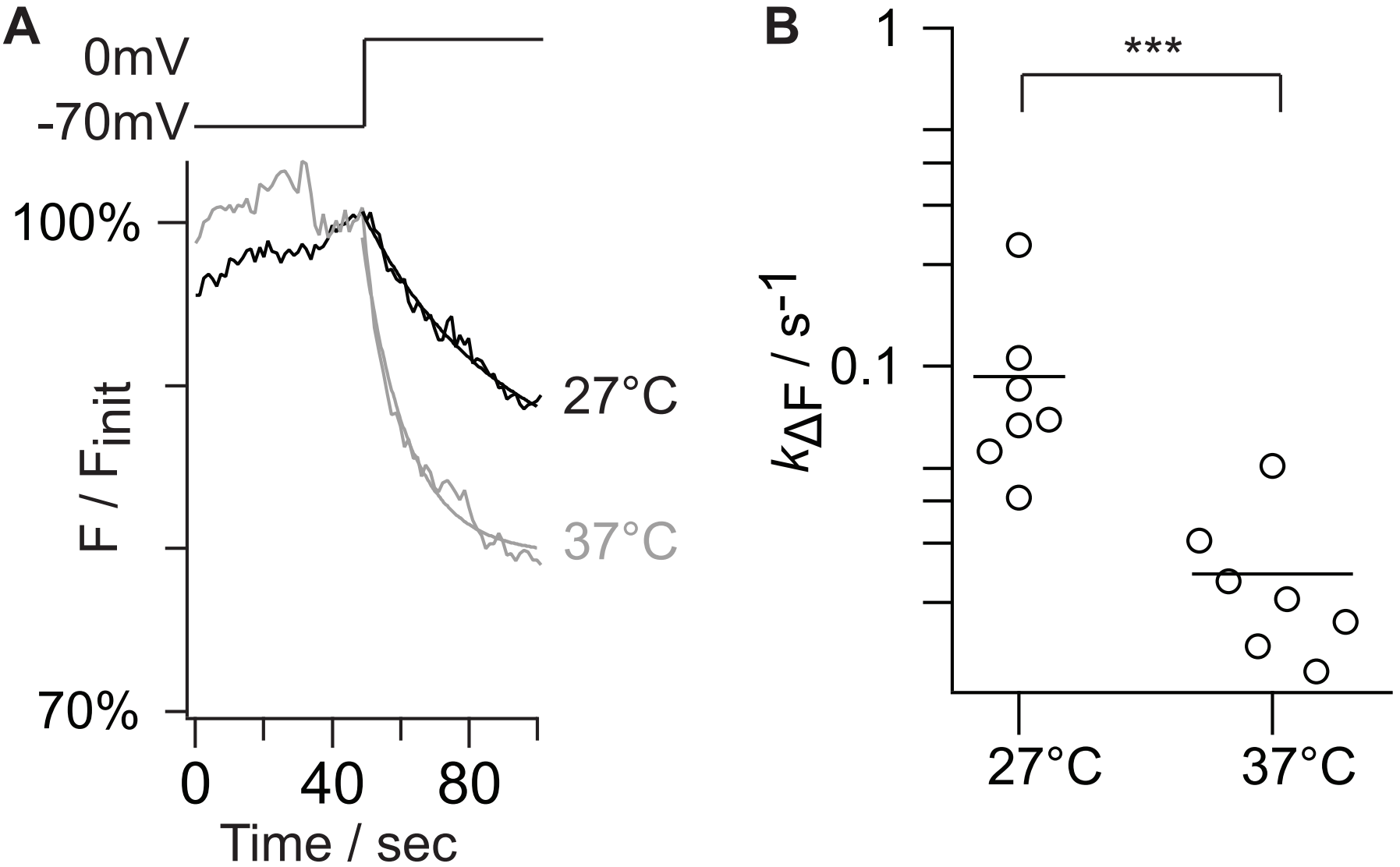

Figure 4

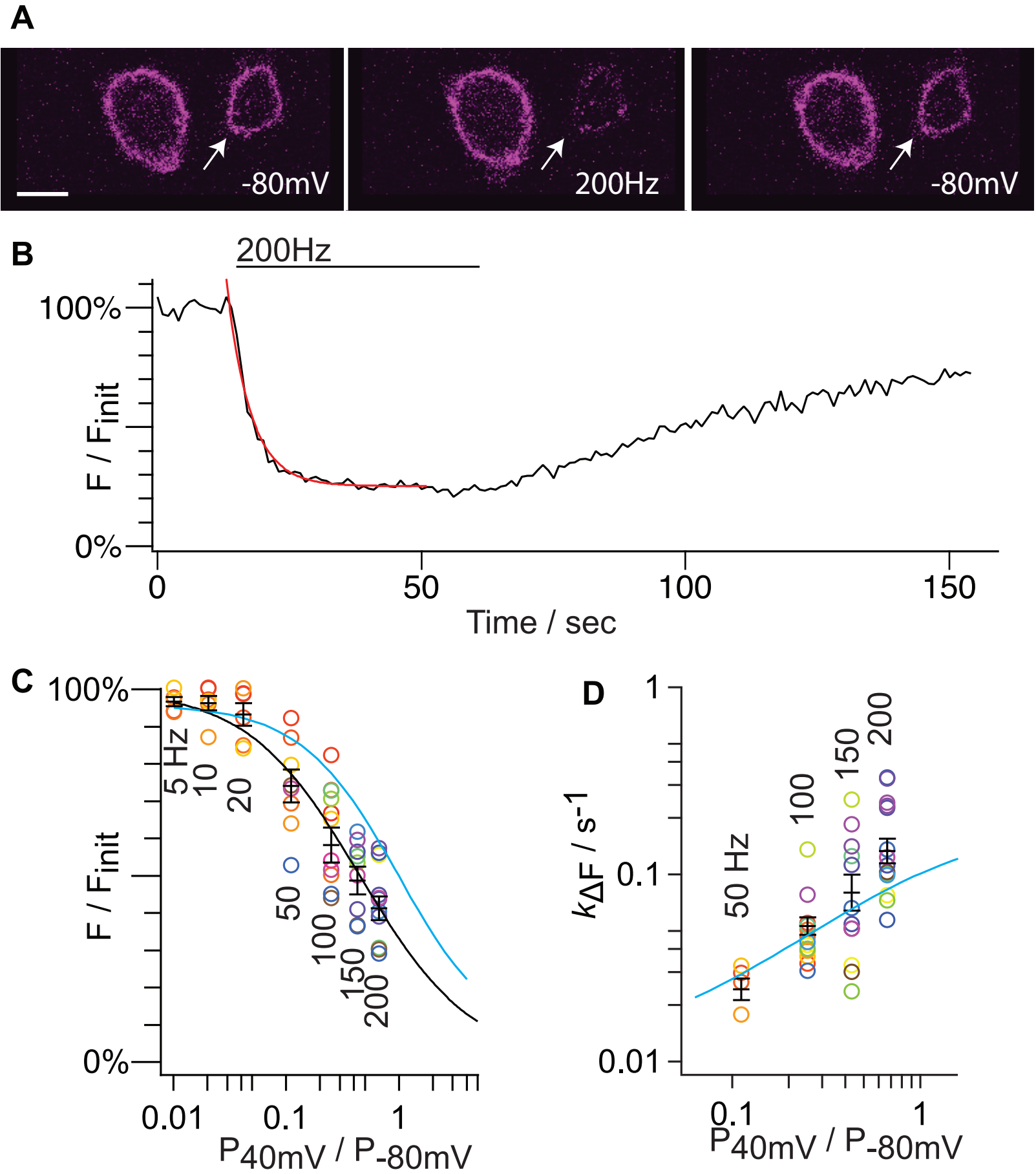
A
-80mV
200Hz
-80mV
B
200Hz
100%
0%
F / Finit
0
50
100
150
Time / sec
C
100%
0%
F / Finit
5 Hz
10
20
50
100
150
200
0.01
0.1
1
P40mV / P-80mV
D
1
0.1
0.01
kΔF / s-1
50 Hz
100
150
200
0.1
1
P40mV / P-80mV

Figure 5

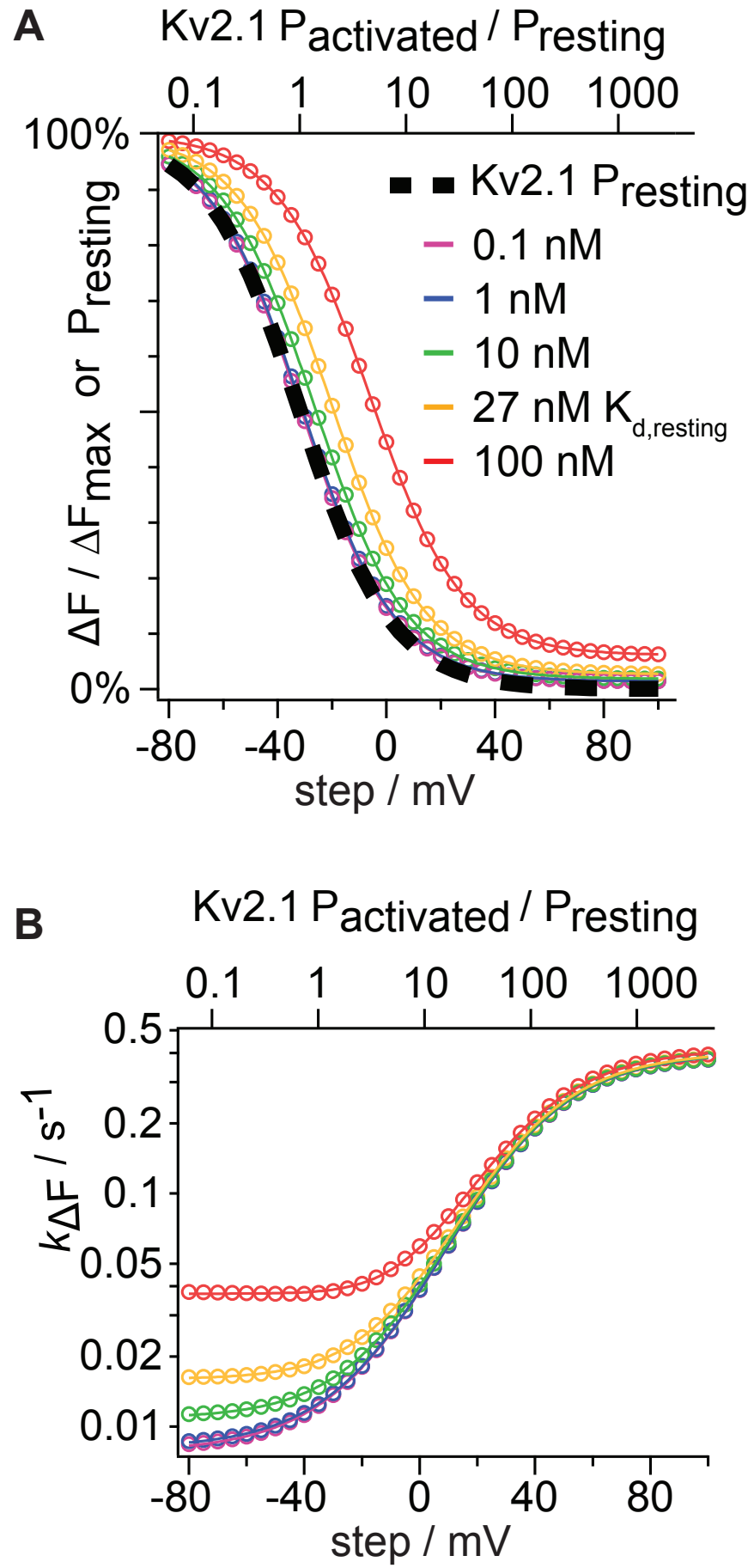
A
Kv2.1 Pactivated / Presting
0.1
1
10
100
1000
100%
0%
ΔF / ΔFmax or Presting
Kv2.1 Presting
0.1 nM
1 nM
10 nM
27 nM Kd,resting
100 nM
-80
-40
0
40
80
step / mV
B
Kv2.1 Pactivated / Presting
0.1
1
10
100
1000
0.5
0.2
0.1
0.05
0.02
0.01
kΔF / s-1
-80
-40
0
40
80
step / mV

Figure 6

A

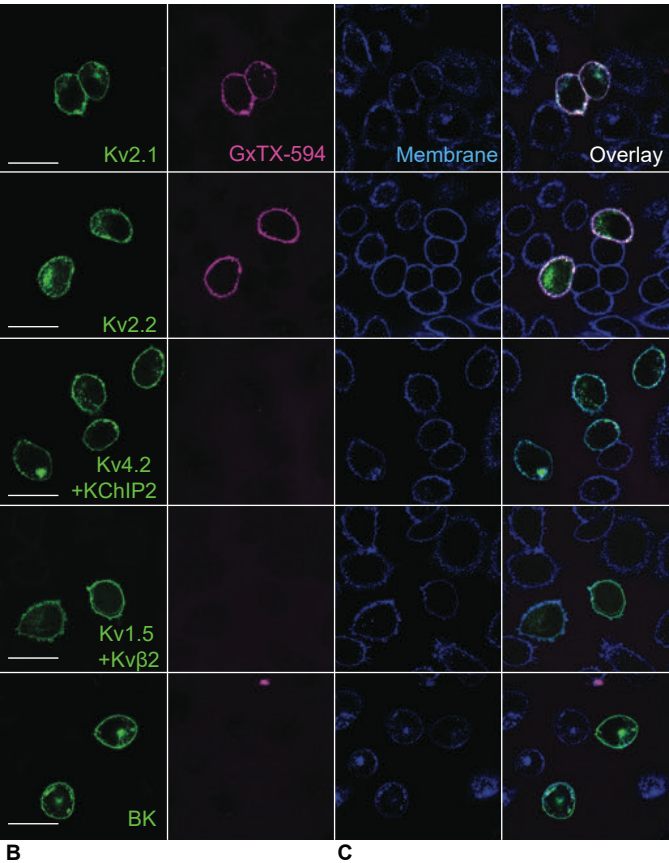
Kv2.1
GxTX-594
Membrane
Overlay
Kv2.2
Kv4.2
+KChIP2
Kv1.5
+Kvβ2
BK

B

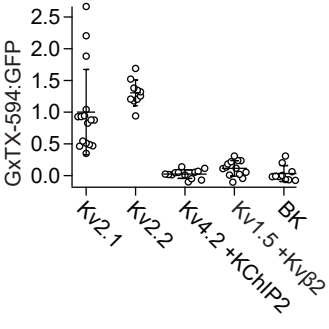
GxTX-594:GFP
2.5
2.0
1.5
1.0
0.5
0.0
Kv2.1
Kv2.2
Kv4.2 +KChIP2
Kv1.5 +Kvβ2
BK

C

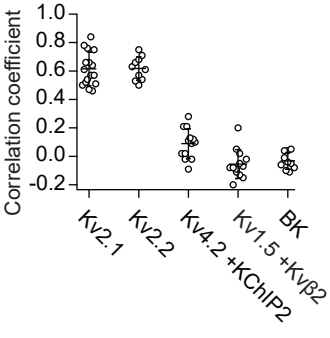
Correlation coefficient
1.0
0.8
0.6
0.4
0.2
0.0
-0.2
Kv2.1
Kv2.2
Kv4.2 +KChIP2
Kv1.5 +Kvβ2
BK

Figure 6 Supplement 1

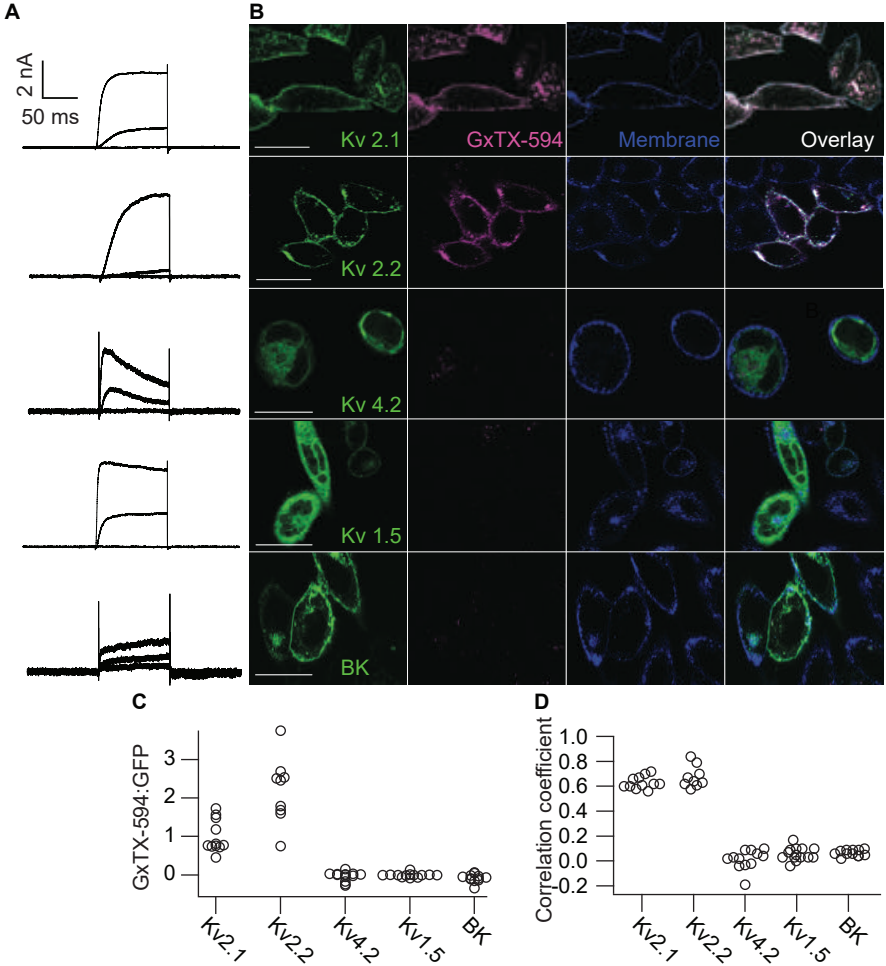

Figure 7

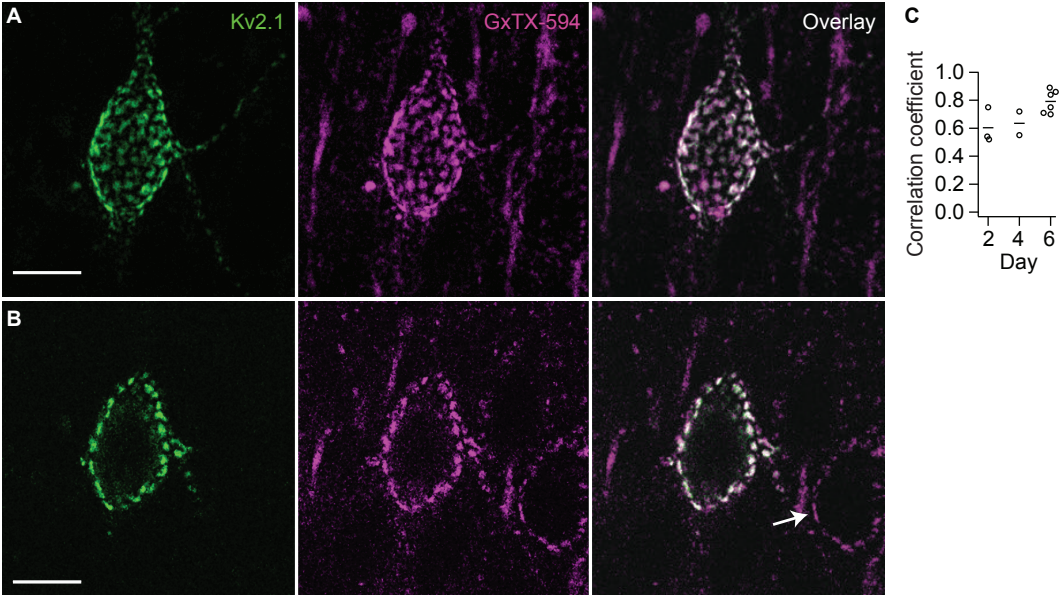
A
Kv2.1
GxTX-594
Overlay
B
C
Correlation coefficient
1.0
0.8
0.6
0.4
0.2
0.0
2
4
6
Day

Figure 7 Supplement 1

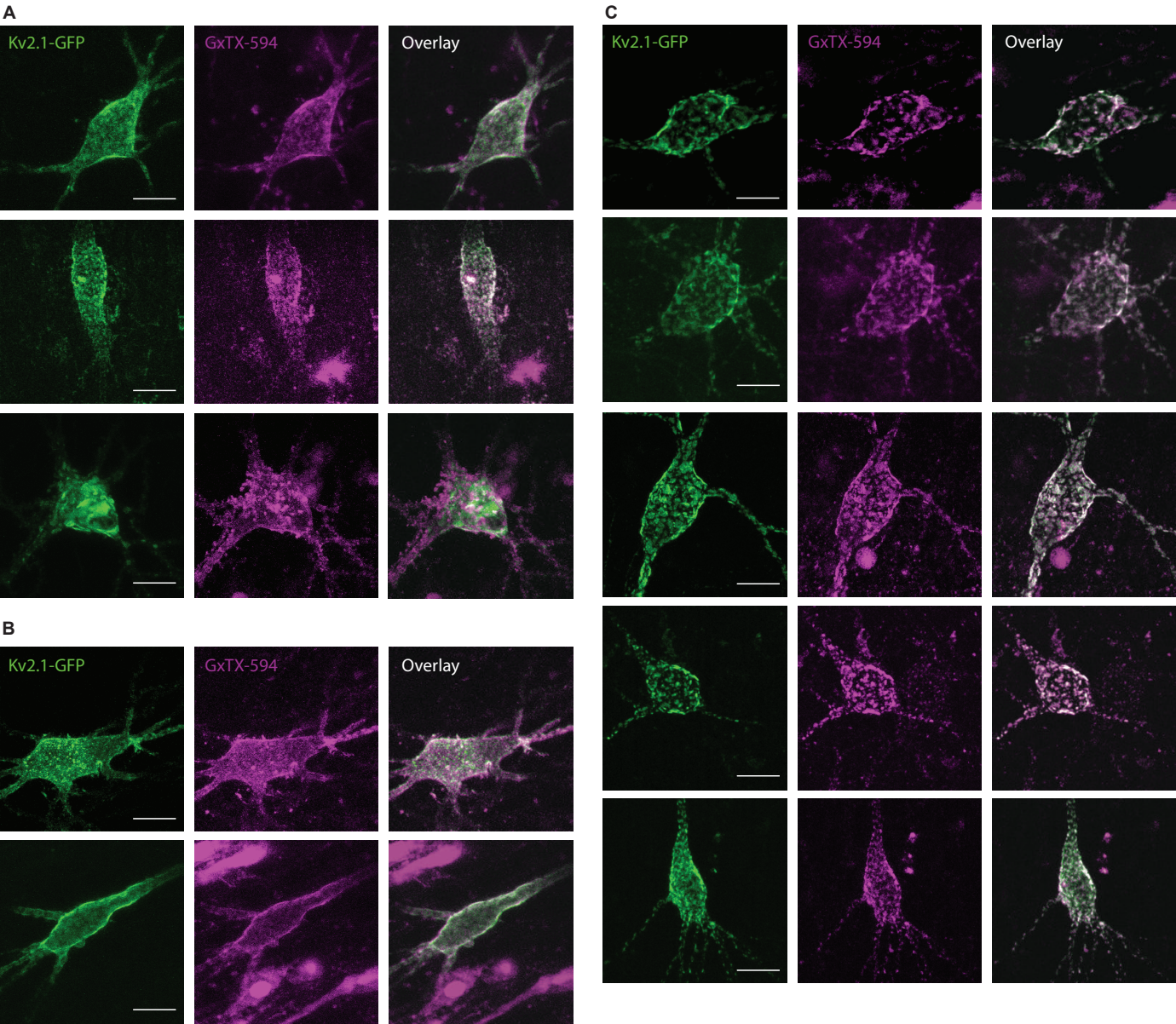

Figure 8

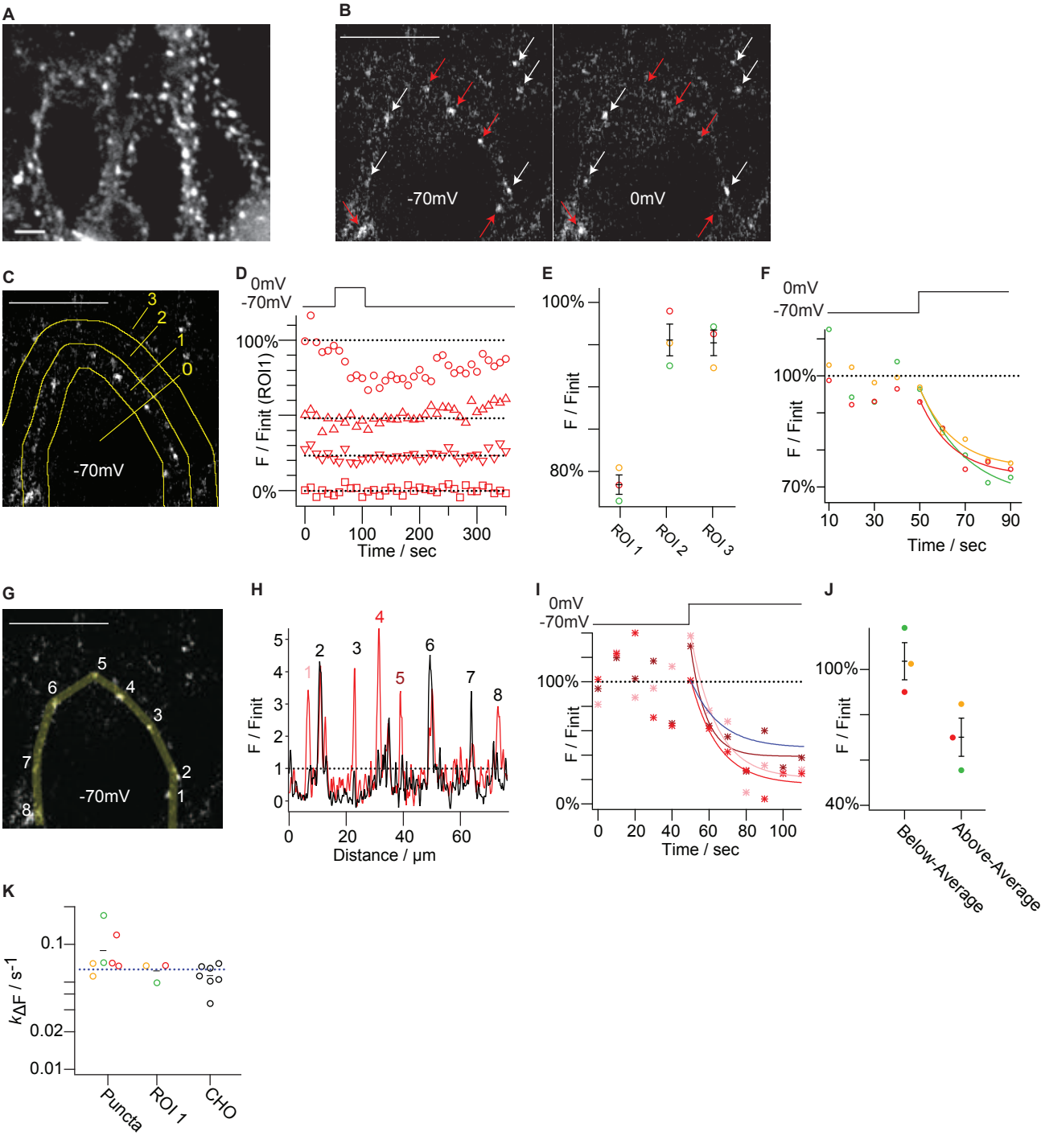
A
B
-70mV
0mV
C
3
2
1
0
-70mV
D
0mV
-70mV
100%
0%
F / Finit (ROI1)
0
100
200
300
Time / sec
E
100%
80%
F / Finit
ROI 1
ROI 2
ROI 3
F
0mV
-70mV
100%
70%
F / Finit
10
30
50
70
90
Time / sec
G
5
6
4
3
7
2
-70mV
1
8
H
1
2
3
4
5
6
7
8
F / Finit
0
20
40
60
Distance / µm
I
0mV
-70mV
100%
0%
F / Finit
0
20
40
60
80
100
Time / sec
J
100%
40%
F / Finit
Below-Average
Above-Average
K
0.1
0.02
0.01
$k_{\Delta F}$ / s^{-1}
Puncta
ROI 1
CHO